Atmos. Meas. Tech. Discuss., 5, 1–60, 2012
www.atmos-meas-tech-discuss.net/5/1/2012/
doi:10.5194/amtd-5-1-2012

Atmospheric Measurement Techniques Discussions

The ACOS X_{CO_2} retrieval algorithm, Part 2: Global X_{CO_2} data characterization

D. Crisp[1], B. M. Fisher[1], C. O'Dell[2], C. Frankenberg[1], R. Basilio[1], H. Bösch[3], L. R. Brown[1], R. Castano[1], B. Connor[4], N. M. Deutscher[5,6], A. Eldering[1], D. Griffith[6], M. Gunson[1], A. Kuze[7], L. Mandrake[1], J. McDuffie[1], J. Messerschmidt[8], C. E. Miller[1], I. Morino[9], V. Natraj[1], J. Notholt[5], D. O'Brien[2], F. Oyafuso[1], I. Polonsky[2], J. Robinson[10], R. Salawitch[11], V. Sherlock[10], M. Smyth[1], H. Suto[7], T. Taylor[2], D. R. Thompson[1], P. O. Wennberg[8], D. Wunch[8], and Y. L. Yung[8]

[1]Jet Propulsion Laboratory, California Institute of Technology, Pasadena, CA, USA
[2]Colorado State University, Fort Collins, CO, USA
[3]University of Leicester, Leicester, UK
[4]BC Consulting, Ltd., Alexandra, New Zealand

[5]University of Bremen, Bremen, Germany
[6]University of Wollongong, Wollongong, NSW, Australia
[7]Japan Aerospace Exploration Agency, Tsukuba, Japan
[8]California Institute of Technology, Pasadena, CA, USA
[9]National Institute for Environmental Studies, Tsukuba, Japan
[10]National Institute of Water & Atmospheric Research, Wellington, New Zealand
[11]University of Maryland, College Park, MD, USA

Received: 24 November 2011 – Accepted: 1 December 2011 – Published: 3 January 2012

Correspondence to: D. Crisp (david.crisp@jpl.nasa.gov)

Published by Copernicus Publications on behalf of the European Geosciences Union.

Abstract

Here, we report preliminary estimates of the column averaged carbon dioxide (CO_2) dry air mole fraction, X_{CO_2}, retrieved from spectra recorded over land by the Greenhouse gases Observing Satellite, GOSAT (nicknamed "Ibuki"), using retrieval methods originally developed for the NASA Orbiting Carbon Observatory (OCO) mission. After screening for clouds and other known error sources, these retrievals reproduce much of the expected structure in the global X_{CO_2} field, including its variation with latitude and season. However, low yields of retrieved X_{CO_2} over persistently cloudy areas and ice covered surfaces at high latitudes limit the coverage of some geographic regions, even on seasonal time scales. Comparisons of early GOSAT X_{CO_2} retrievals with X_{CO_2} estimates from the Total Carbon Column Observing Network (TCCON) revealed a global, −2 % (7–8 parts per million, ppm, with respect to dry air) X_{CO_2} bias and 2 to 3 times more variance in the GOSAT retrievals. About half of the global X_{CO_2} bias is associated with a systematic, 1 % overestimate in the retrieved air mass, first identified as a global +10 hPa bias in the retrieved surface pressure. This error has been attributed to errors in the O_2 A-band absorption cross sections. Much of the remaining bias and spurious variance in the GOSAT X_{CO_2} retrievals has been traced to uncertainties in the instrument's calibration, oversimplified methods for generating O_2 and CO_2 absorption cross sections, and other subtle errors in the implementation of the retrieval algorithm. Many of these deficiencies have been addressed in the most recent version (Build 2.9) of the retrieval algorithm, which produces negligible bias in X_{CO_2} on global scales as well as a ∼30 % reduction in variance. Comparisons with TCCON measurements indicate that regional scale biases remain, but these could be reduced by applying empirical corrections like those described by Wunch et al. (2011). We recommend that such corrections be applied before these data are used in source sink inversion studies to minimize spurious fluxes associated with known biases. These and other lessons learned from the analysis of GOSAT data are expected to accelerate the delivery of high quality data products from the Orbiting Carbon Observeratory-2 (OCO-2), once that satellite is successfully launched and inserted into orbit.

AMTD

5, 1–60, 2012

1 Introduction

Space-based remote sensing observations hold substantial promise for quantifying surface fluxes of CO_2 and other greenhouse gases on regional scales over the globe. These observations are expected to complement, rather than replace those from the existing surface-based greenhouse gas monitoring network (e.g. Conway et al., 2011) by providing improved spatial coverage and sampling densities in data-poor regions. High resolution spectra of reflected sunlight within short-wave infrared (SWIR) CO_2 bands are well suited for this application because these data can be analyzed to yield estimates of the column averaged CO_2 dry air mole fraction, X_{CO_2}, with their greatest sensitivity to CO_2 variations near the surface (O'Brien and Rayner, 2002; Kuang et al., 2002; Olsen and Randerson, 2004; Crisp et al., 2004, 2008; Miller et al., 2007). The principal challenge for this measurement approach is the need for high precision and low bias on regional to global scales to resolve and quantify the small (0.25 % to 2 %) variations in X_{CO_2} associated with surface sources and sinks on these spatial scales (Miller et al., 2007).

The Japanese Greenhouse gases Observing Satellite (GOSAT) and the NASA Orbiting Carbon Observatory (OCO) were the first space-based sensors designed specifically to measure CO_2 with the sensitivity, spatial resolution, and geographic coverage needed to quantify CO_2 sources and sinks on regional scales at monthly intervals (Crisp et al., 2004, 2008; Hamazaki et al., 2005; Kuze et al., 2009a). Both satellites implemented high resolution spectrometers optimized to return high precision measurements of reflected sunlight within CO_2 and molecular oxygen (O_2) absorption bands at SWIR wavelengths. GOSAT was successfully launched on 23 January 2009, and has been returning global measurements of X_{CO_2} since June 2009 (Nakajima et al., 2010; Watanabe et al., 2010). The OCO project suffered a major setback on 24 February 2009 when the satellite was lost due to a launch vehicle malfunction. In early 2010, a replacement mission, called OCO-2, was authorized by NASA, with a target launch readiness date in February 2013.

AMTD
5, 1–60, 2012

The OCO science and GOSAT project teams collaborated closely during the development phases of these missions. The primary objective of this collaboration was to facilitate the combined use of OCO and GOSAT retrievals in CO_2 flux inversion studies by cross calibrating the OCO and GOSAT instruments and developing a common approach for validating their X_{CO_2} products (Crisp, 2009; Nakajima et al., 2010). Immediately after the loss of OCO, the GOSAT project team invited the OCO science team to join their efforts to analyze GOSAT data. NASA responded by reformulating the OCO science team as the Atmospheric CO_2 Observations from Space (ACOS) team. The ACOS team has since worked closely with the GOSAT project team. The combined ACOS/GOSAT team has conducted annual vicarious calibration campaigns over Railroad Valley, NV to validate the on-orbit radiometric calibration of the GOSAT instruments (Kuze et al., 2009b), compared estimates of X_{CO_2} retrieved from GOSAT soundings using the ACOS/OCO-2 algorithm with those generated by the GOSAT product team (Watanabe et al., 2008, 2010; Yoshida et al., 2010), and validated GOSAT X_{CO_2} retrievals against ground-based remote sensing observations collected by Fourier transform spectrometers in the Total Carbon Column Observing Network (TCCON; Wunch et al., 2011).

This is the third in a series of papers describing the algorithms and GOSAT X_{CO_2} data products developed by the ACOS team. Paper I presents methods for evaluating bias in global X_{CO_2} data products using TCCON data (Wunch et al., 2011). Paper II describes the ACOS X_{CO_2} retrieval algorithm and its validation against synthetic data (O'Dell et al., 2011). Here, we summarize the lessons learned from our efforts to retrieve X_{CO_2} from GOSAT soundings collected over land using Build 2.8 (B2.8) of the ACOS X_{CO_2} retrieval algorithm. We also present preliminary results from the next version of the algorithm, Build 2.9 (B2.9), which incorporates many of these insights. The B2.8 product includes all cloud-free GOSAT soundings collected between 4 April 2009 and 20 April 2011. This product was delivered to the MIRADOR portal on the NASA Goddard Earth Sciences Data and Information Services Center (GES DISC; http://mirador.gsfc.nasa.gov/), starting in December 2010. B2.9 deliveries to the

AMTD
5, 1–60, 2012

GES DISC were initiated in mid-November 2011.

2 GOSAT mission overview

The GOSAT mission objectives are described by Yokota et al. (2004) and Hamazaki et al. (2004). The mission design is described in by Nakajima et al. (2010) and the instruments are described in greater detail by Kuze et al. (2009a, b). Here we summarize the mission design, instrument, and calibration issues needed to understand the ACOS/GOSAT X_{CO_2} data product. GOSAT was developed jointly by the Japan Aerospace Exploration Agency (JAXA), the Ministry of the Environment (MOE) Japan, and the National Institute for Environmental Studies (NIES) Japan. The GOSAT project team consists of scientists and engineers at JAXA and NIES. GOSAT flies in a 666 km altitude, 98° inclination, sun-synchronous orbit with a 12:49 pm nodal crossing time and a three-day (44-orbit) ground track repeat cycle. The satellite carries two instruments. The first is the **T**hermal **A**nd **N**ear infrared **S**ensor for carbon **O**bservations-**F**ourier **T**ransform **S**pectrometer, TANSO-FTS. This double pendulum interferometer records reflected sunlight in O_2, CO_2, and CH_4 absorption bands at SWIR wavelengths between 0.758 and 2.08 µm. It also measures thermal emission in a broad (700 to 1800 cm^{-1}, or 5.56 to 14.3 µm) band to retrieve water vapor (H_2O), ozone (O_3), and mid-tropospheric CO_2 and CH_4. The second instrument is the TANSO **C**loud and **A**erosol **I**mager (TANSO-CAI), a high spatial resolution imager designed to facilitate the detection of clouds and optically thick aerosols within the TANSO-FTS field of view. The NIES GOSAT project uses TANSO-CAI results in the cloud screening algorithm for the official GOSAT X_{CO_2} product (Watanabe et al., 2008; Yokota et al., 2009; Yoshida et al., 2011). The ACOS team has used TANSO-CAI data to validate the ACOS cloud screening algorithm (Taylor et al., 2011); however these data are not used in the ACOS X_{CO_2} retrieval algorithm and are not considered further here.

AMTD
5, 1–60, 2012

2.1 Characteristics of GOSAT TANSO-FTS data

The ACOS X_{CO_2} retrieval algorithm uses high resolution spectra of reflected sunlight collected by the TANSO-FTS within its three SWIR bands. The target species, spectral range, and spectral resolution of each band are summarized in Table 1. All three SWIR bands were designed to yield a signal-to-noise ratio (SNR) of ~300 over a surface with a Lambertian albedo of 30 %, illuminated by the sun at a solar zenith angle of 30°. On-orbit calibration tests indicate that all three of the SWIR bands exceed their SNR requirements (Kuze et al., 2009b).

To improve its dynamic range, TANSO-FTS records interferograms with one of two gains in the detector and analog signal chain. Medium Gain (Gain M) is used over bright desert surfaces (e.g. Sahara, central Australia, and Railroad Valley, Nevada). High Gain (Gain H) is used over all other surfaces. Interferograms for each band are recorded in two orthogonal linear polarizations, designated "P" and "S", whose polarization axes are aligned roughly along and perpendicular to the direction of spacecraft motion, respectively. The instrument supports interferogram scan times of 1.1, 2, and 4 s. A 4-s scan time has been used for all routine TANSO-FTS science observations.

TANSO-FTS collects interferograms within a 0.0158-radian diameter, circular, instantaneous field of view (IFOV) yielding footprints that are ~10.5 km in diameter at nadir. A two-axis pointing mirror is used to direct this IFOV within ±35° of nadir in the cross-track direction and within ±20° of nadir along the spacecraft ground track (Shiomi et al., 2008). A camera installed in the TANSO-FTS and co-bore-sighted with its IFOV is used to monitor the actual position of the IFOV (Kuze et al., 2009a). The pointing mechanism includes pre-programmed 1, 3, 5, 7, and 9-point cross-track scan modes, a sun-glint tracking mode, and a specific point mode. It also provides image motion compensation (IMC) during individual 4-s interferogram scans. The 5-point cross-track scan mode yields footprints separated by ~158 km cross-track and ~152 km along track. The 3-point cross-track scan mode yields footprints that are separated by ~263 km cross-track and ~283 km along-track (Watanabe et al., 2008). In this mode, each footprint is sampled 3 times. The 5-point cross-track scan mode was used for routine science

AMTD
5, 1–60, 2012

observations between 4 April 2009 and 31 July 2010. On 1 August 2010, the 5-point mode was replaced with the 3-point cross-track pattern to improve the pointing stability during the TANSO-FTS 4-second scan time. This sampling pattern has been used for all subsequent routine science observations.

In sun glint mode, the pointing mechanism targets the sun-glint spot to increase the signal to noise ratio. This mode is used over the ocean at latitudes within 20° of the sub-solar latitude. Prior to 1 August 2010, IMC was not used for glint observations, but has been used since that date. Finally, the scan mechanism can point to stationary surface targets, acquiring up to 3 exposures as GOSAT flies overhead. This mode is routinely used to target vicarious calibration sites, such as Railroad Valley, Nevada (Kuze et al., 2011), and validation sites, including TCCON stations (Washenfelder et al., 2006; Wunch et al., 2010, 2011; Messerschmidt et al., 2011; Deutscher et al., 2010).

2.2 TANSO-FTS calibration issues

While the TANSO-FTS has been performing well, on-orbit calibration and validation activities have revealed subtle radiometric, geometric, and spectroscopic calibration issues that introduce error in the retrievals of X_{CO_2}. For example, vicarious calibration campaigns and on-orbit radiometric calibration activities (Kuze et al., 2009b, 2011) reveal time dependent reductions in the throughput of the instrument. The largest changes are seen in Band 1 (O_2 A-band). When compared to the pre-launch calibration results, the Band 1 throughput had decreased by 11 ± 7 % as of June 2009, and by an additional ~3 % per year since that time. Degradation in bands 2 and 3 has been a factor of 3 to 4 smaller. The impact of these radiometric calibration changes on X_{CO_2} retrievals is assessed below.

Images acquired by the camera installed inside the TANSO-FTS indicate that the pointing mechanism has systematic offsets that change with time (Kuze et al., 2011). In general, larger errors are seen in the along-track direction. From April 2009 through July 2010, when the 5-point cross-track scan mode was used, typical cross-track

AMTD
5, 1–60, 2012

pointing and along-track pointing errors were <0.25° (~3 km at nadir) for most points, but every 5th point (scan points 0 and 5) had along-track errors as large as 0.9° (~10 km at nadir). Since August 2010, the 3-point cross-track scan has yielded pointing errors that are more consistent from sounding to sounding, with amplitudes between 5 and 6 km in the down-track direction and ~3 km to the left of the intended target in the cross-track direction. The cause of these errors is still under investigation.

Three factors have compromised the TANSO-FTS spectroscopic calibration. The first is caused by scan speed instabilities in the interferometer associated with satellite- and instrument-induced micro-vibrations (Suto et al., 2011). These instabilities produced their largest effects on the Gain M observations collected over bright surfaces. This anomaly has been characterized and can be corrected by re-sampling the interferogram. This correction has been applied to all Level 1B data collected after 24 November 2010. It has not yet been applied to the earlier data.

The second issue is a weak (1–2 %) non-linearity in the response to the intensity of the incident radiation, which was first inferred from observations of Fraunhofer line depths over Antarctica (Frankenberg et al., 2011b). The TANSO-FTS Band 1 (O_2 A-band) interferograms are affected most by this artifact. The source of this non-linearity has recently been traced to the Band 1 analog signal chain and analog to digital converters and is currently being characterized and calibrated (Suto et al., 2011). When the Band 1 interferograms are transformed to yield O_2 A-band spectra, the non-linearity introduces intensity-dependent zero level offsets and other artifacts that compromise the radiometric and spectroscopic calibration. The impact of this non-linearity on X_{CO_2} retrievals is assessed below.

Finally, the spectrally dependent radiance correction factors used to convert the TANSO-FTS Level 1B spectra from engineering units (volts) to radiometric units ($W\,cm^{-2}\,str^{-1}\,(cm^{-1})^{-1}$) introduce small, spectrally dependent errors in the spectra. The conversion coefficients used for B2.8 were derived from laboratory measurements acquired prior to launch, along open atmospheric paths. Weak absorption by O_2, CO_2, and possibly other gases introduced small spectrally-dependent artefacts in these

AMTD
5, 1–60, 2012

conversion files. These errors have been corrected in the latest version of the conversion factors delivered by the GOSAT calibration team.

3 The ACOS GOSAT X_{CO_2} retrieval approach

The ACOS GOSAT X_{CO_2} retrieval approach evolved from the OCO retrieval algorithm, which is based on Bayesian optimal estimation (Rodgers, 2000; Bösch et al., 2006; Connor et al., 2008; Bösch et al., 2011; O'Dell et al., 2011). This algorithm and its input data are evolving rapidly as we incorporate lessons learned from the GOSAT data processing. The architecture and performance of algorithm builds 2.8 and 2.9 are documented by Crisp et al. (2010) and O'Dell et al. (2011). Only those aspects of the retrieval algorithm directly relevant to the interpretation of the GOSAT TANSO-FTS retrievals are discussed here.

The ACOS/OCO-2 X_{CO_2} retrieval algorithm incorporates the following major components: (i) a pre-processing step to identify cloud-free soundings that are likely to converge and to initialize the surface-atmosphere state, (ii) a "forward" radiative transfer model to generate synthetic spectra, (iii) a TANSO-FTS instrument model to simulate the observed spectral resolution, (iv) an inverse model to update the surface-atmosphere state, and (iv) a post-processing screening step to identify and reject bad retrievals.

For B2.8 and B2.9, the preprocessor module rejects all soundings collected at solar zenith angles greater than 85° because these retrievals often fail to converge or produce large systematic errors. The remaining soundings are then screened for optically thick clouds using the O_2 A-band cloud screening method described by Taylor et al. (2011).

Spectra that pass the pre-screening tests are passed to the X_{CO_2} retrieval algorithm. Given an initial guess for the atmospheric and surface state and the solar illumination and observing geometry for a specific TANSO-FTS sounding, the forward radiative transfer model generates synthetic radiance spectra within the 0.76 µm O_2 A-band

AMTD
5, 1–60, 2012

and for the two CO_2 bands centered near 1.61 and 2.06 µm. Due to its heritage, the ACOS retrieval algorithm uses the spectral ranges sampled by the OCO instrument (Table 1) rather than the full spectral ranges of the TANSO-FTS SWIR bands. Absorption cross-sections for CO_2, H_2O, and O_2 within these spectral ranges are read from pre-computed tables, that were generated by methods documented in the OCO-2 Algorithm Theoretical Basis Document (Crisp et al., 2010). To account for scattering and absorption by clouds and aerosols, the retrieval algorithm includes absorption and scattering by the four prescribed airborne particle types given in O'Dell et al. (2011). The optical depth profile for each particle type is retrieved for each sounding. This approach for retrieving cloud and aerosol optical properties is quite different from those implemented by the NIES GOSAT project team (Yokota et al., 2009; Yoshida et al., 2010) and by Butz et al. (2011), and may introduce differences in X_{CO_2} retrievals.

Given high-resolution, polarization-dependent synthetic spectra of the 0.76 µm O_2 A-band (ABO2), the weak 1.61 µm CO_2 band (WCO2), and the strong 2.06 µm CO_2 band (SCO2), the ACOS GOSAT instrument model performs three operations to simulate the TANSO-FTS spectral resolution and polarization dependence. First, the mean intensity at each spectral point in each SWIR spectral band is estimated by multiplying each Stokes parameter by the associated element in the instrument Mueller matrix (Kuze et al., 2009a; O'Brien et al., 2011) to correct for the polarization introduced by the instrument and its pointing mechanism. The mean intensity for each TANSO-FTS sample is then estimated by convolving the simulated spectrum with the instrument line shape function to match the spectral resolution and dispersion. These values are compared to the average of the TANSO FTS measurement in its P and S polarizations (O'Dell et al., 2011), yielding a quantity nearly identical to the total unpolarized intensity (O'Brien et al., 2011).

To estimate X_{CO_2}, the ACOS B2.8 algorithm performs a simultaneous retrieval using all 3 TANSO-FTS SWIR spectral bands to return estimates of ~113 atmospheric and surface state properties, as well as a small wavelength offset for each band (O'Dell et al., 2011). For B2.9, we also retrieve a radiance offset in the O_2 A-band to mitigate

AMTD
5, 1–60, 2012

errors associated with the instrument's non-linear response to the incident radiance level in Band 1, the utility of which was recently demonstrated (Butz et al., 2011).

To evaluate the quality of each X_{CO_2} estimate and facilitate the use of these data in source-sink inversion models, the retrieval algorithm also records the pressure weighting functions, column averaging kernels, and a posteriori error estimates for the level-dependent CO_2 volume mixing ratios, surface pressure, and X_{CO_2} for each converged sounding. Other diagnostic quantities recorded include the retrieval outcome (convergence reached), the signal to noise ratio and goodness of fit (χ^2) in each SWIR band, the number of iterations, and diverging steps steps, and the estimated X_{CO_2} uncertainty. These diagnostic quantities are used in a post-screening step to define a sounding quality flag.

4 X_{CO_2} retrievals from GOSAT data using B2.8

Our initial efforts to retrieve the global distribution of X_{CO_2} from GOSAT data produced promising results, qualitatively reproducing many expected features, including the latitudinal gradients and their variations over the seasonal cycle. However, comparisons of ACOS GOSAT B2.8 X_{CO_2} estimates with TCCON X_{CO_2} retrievals revealed significant biases in the B2.8 products. All cloud-screened ACOS GOSAT B2.8 X_{CO_2} retrievals acquired over land at solar zenith angles <85° for July 2009 are shown as grey triangles in Fig. 1. The subset of those soundings that also passed a series of post-screening filters (described in greater detail below) are over-plotted as green triangles. Monthly means of TCCON measurements from 8 sites (Table 2) between Lauder, New Zealand (45° S) and Bialystok, Poland (53.2° N) are shown as red diamonds with error bars indicating the standard deviation of the measurements over each site for July 2009.

When averaged into 10° wide zonal bins, the screened ACOS GOSAT retrievals (blue triangles with 1-σ error bars) reproduce much of the latitudinal structure in X_{CO_2}. However, the space-based values are systematically ~2 % (7 to 8 ppm) lower than the TCCON values for the range of sampled latitudes. Similar results are seen for all

AMTD
5, 1–60, 2012

months included in the B2.8 product. The ACOS GOSAT retrievals also show substantially more variability in X_{CO_2} than is seen at the TCCON sites. Some of this variability can be attributed to the lower intrinsic SNR of the GOSAT measurements and the fact that the ACOS GOSAT error bars represent results for 10° wide zonal bands, rather than individual sites, but much of it is likely to be spurious. Factors contributing to the bias and excess variance in the ACOS GOSAT X_{CO_2} retrievals are explored below.

5 Diagnosing the causes of the X_{CO_2} bias and excess variability

About half of the bias between the ACOS GOSAT and TCCON X_{CO_2} retrievals is contributed by a ~1 % high bias in the retrieved O_2 column abundance, which is manifested as a global ~10 hPa overestimate in the retrieved surface pressure (Fig. 2a). This bias is primarily due to an underestimate of the O_2 A-band absorption cross sections used in the B2.8 algorithm, and a compensating overestimate in air mass. These errors are not seen in routine TCCON X_{CO_2} retrievals because the standard TCCON GFIT algorithm uses the 1.27 µm $O_2^1\Delta_g$ band rather than the O_2 A-band to estimate the dry air column (Wunch et al., 2010, 2011). When the O_2 A-band is used to retrieve X_{CO_2} from TCCON spectra, with either the standard TCCON GFIT algorithm or the ACOS/OCO-2 algorithm, we obtain a similar bias. The remainder of the bias between the ACOS GOSAT and TCCON retrievals is associated with unresolved instrument calibration uncertainties, differences in the O_2 and CO_2 absorption cross-sections, and errors or oversimplifications in the ACOS/OCO-2 retrieval algorithm.

Several factors contribute spurious variability in the ACOS GOSAT X_{CO_2} retrievals. Some of it is likely due to contamination by optically thick clouds and aerosols that were missed by the cloud screening process (O'Dell et al., 2011). Optical path biases can also be introduced by oversimplifications in the optical properties or systematic errors in the retrieved distribution of optically thin ($\tau \leq 0.15$) clouds and aerosols. TCCON retrievals are less sensitive to these errors because the TCCON spectrometers make

AMTD
5, 1–60, 2012

direct observations of the solar disk, eliminating any significant contribution of scattered light in the spectra.

The ACOS/OCO-2 algorithm assumes that the prescribed pointing geometry is exact. Pointing errors associated with uncertainties in the geometric calibration of the TANSO-FTS can therefore contribute to the observed scatter by introducing quasi-random errors in the atmospheric optical path length. To compensate for these optical path errors, the algorithm will adjust the number density or pressure to optimize the spectral fits, introducing subtle biases in individual retrievals. These errors are likely to be largest in areas with rough topography, where a small pointing error can yield a large error in path length.

The 1 % surface pressure bias can also contribute to scatter in the retrieved X_{CO_2}, because the cost function minimized by the inverse algorithm (Connor et al., 2008; O'Dell et al., 2011) pulls retrievals with poor spectral fits toward the unbiased ECMWF surface pressure prior more strongly than it does those with smaller spectral residuals. Other factors, including low SNR in one or more bands, poor or diverging spectral fits, or correlations between retrieved state vector quantities can also introduce scatter (O'Dell et al., 2011). Many of these issues can be identified in the post screening process. However, even the soundings that pass all screening criteria used in B2.8 exhibit 3 to 5 times more variability in X_{CO_2} than that seen in the TCCON retrievals.

5.1 Impact of time-dependent variations in the TANSO-FTS radiometric calibration

On-orbit and vicarious calibration campaigns have revealed a reduction in the throughput of the TANSO-FTS over time (Kuze et al., 2011). The effects on these throughput changes on the retrieved X_{CO_2} product is illustrated in Fig. 3 for soundings collected over Australia. ACOS GOSAT products delivered prior to B2.8 used radiometric calibration factors based on pre-launch measurements with no degradation (blue line). Preliminary estimates of the time-dependent radiometric calibration correction factors were delivered by the JAXA GOSAT project team in August of 2010. These values

AMTD
5, 1–60, 2012

were incorporated into the B2.8 production run (black line in Fig. 3). These calibration corrections reduced the negative X_{CO_2} bias by amounts that varied from ~1 ppm in April 2009 to ~1.5 ppm in December 2010. Revised estimates of the time-dependent radiometric calibration factors were delivered by the GOSAT Calibration Team in late 2010 (Kuze et al., 2011), but it was too late to incorporate these factors into the B2.8 product. Recent tests show that these revised parameters reduce the X_{CO_2} bias by an additional 0.5 ppm early in the mission, but this difference decreases with time (red line in Fig. 3). These revised calibration factors were used in the B2.9 products described below.

The implementation of this time-dependent calibration correction also introduced a subtle artifact in the B2.8 product. The revised calibration parameters were applied to the radiances, but not to the corresponding instrument noise estimates. This error introduces a spurious, time-dependent increase in the χ^2 values in all three SWIR bands over time. To prevent the post-processing filter on χ^2 from screening out progressively more data each month, the B2.8 post-screening filters were modified to accommodate a linear increase of χ^2 over time. This implementation error was corrected in B2.9.

5.2 Impact of spectroscopic uncertainties on bias and scatter

Other sources of the observed bias and scatter in the ACOS GOSAT retrievals include uncertainties in the instrument radiometric linearity or spectroscopic calibration (Kuze et al., 2010, 2011; Suto et al., 2011), poor spectral fits associated with errors or oversimplifications in the in absorption line databases, and the neglect of chlorophyll fluorescence (Frankenberg et al., 2011). The relative roles of these factors can be discriminated to some extent by comparing the wavelength-dendent structure of the TANSO-FTS spectral residuals with that seen in uplooking atmospheric absorption spectra collected by TCCON or gas absorption cell spectra acquired in the laboratory. Residuals that are common to laboratory, TCCON, and TANSO-FTS spectra are most likely due to uncertainties in the wavelength-dependent absorption cross sections of CO_2 or O_2. Spectral residuals common to TCCON and TANSO-FTS spectra, but not

AMTD
5, 1–60, 2012

seen in laboratory spectra, are likely to be contributed primarily by uncertainties in the abundance or distribution (or neglect) of atmospheric absorbers, or errors in the assumed top-of-atmosphere solar spectrum. Spectral residuals seen only in TANSO-FTS fits are most likely to be caused by calibration uncertainties, errors or oversimplifications in the surface or aerosol optical properties, or other shortcomings in the retrieval algorithm.

Typical spectral fits and fit residuals for each of the 3 TANSO-FTS SWIR spectral bands are shown in Fig. 4. Here, the spectral residuals have peak-to-peak amplitudes of ~1 %, or 1.5 to 2.5 times the intrinsic instrument noise level. These results are for a single, high SNR sounding obtained near the Lamont, Oklahoma TCCON station. However, the residuals show features that persist in averages of large numbers of spectra collected on regional to continental scales.

For the WCO2 band, fits to both TANSO-FTS and TCCON spectra show persistent residuals that are generally smaller than those in the other 2 bands. The largest of these residuals are associated with poorly fit solar lines. Both TANSO-FTS and TCCON residuals show a 0.5 to 1 % variation in the continuum that is not seen in laboratory spectra. This error may be associated with deficiencies in the solar continuum or in the neglect of continuum absorbers in the Earth's atmosphere. In contrast, the most persistent residuals in the ABO2 and SCO2 bands are well correlated with the band structure. For these two bands, similar spectrally-dependent residuals are seen in fits to TCCON X_{CO_2} spectra as well as in laboratory spectra, suggesting that they are caused primarily by deficiencies in the O_2 and CO_2 gas absorption cross sections.

Recent advances in the laboratory measurements and analysis techniques have produced substantial improvements in our understanding of the CO_2 absorption cross sections in both the WCO2 and SCO2 bands. Improved laboratory techniques include more precise measurements of pressures (±0.01 Torr), temperatures (±0.1 K), isotopic content of the samples (±0.05 %), and optical path lengths (0.1 %) of the absorption cells, as well as higher SNR (2000:1), and reduced uncertainty in the instrument line shape. These methods allow the detection and quantification of line positions,

AMTD
5, 1–60, 2012

strengths, widths, pressure shifts, and temperature dependence with unprecedented accuracy (Toth et al., 2006a, b, 2007a, b; 2008a, b). The laboratory data are being analyzed with advanced multi-spectrum analysis techniques that fit dozens of spectra simultaneously, providing a self-consistent description of the line parameters (positions, strengths, widths, shifts, and temperature dependence) in the presence of line mixing for a speed-dependent Voigt line shape (Devi et al., 2007; Benner et al., 2009, 2011). These line parameters produce CO_2 absorption cross sections that yield much smaller residuals in fits to laboratory spectra (Fig. 5a). Their use in the ACOS/OCO-2 algorithm produces somewhat smaller reductions fitting residuals in fits to GOSAT spectra (Fig. 5b). Some of the remaining residuals have been traced to poorly fit solar lines and inadequately fit water vapor lines. The remaining residuals that are well correlated with the CO_2 absorption may be associated with inadequacies in the treatment of line mixing or the far wings of CO_2 lines, or other atmospheric absorption processes not present in the laboratory measurements, and neglected here, such as water vapor continuum absorption.

A comparison of the O_2 A-band residuals for a Lamont TCCON spectrum and an average of nearby ACOS GOSAT retrievals is shown in Fig. 6. For the weakest lines at the short wavenumber end of this band ($<13\,050\,cm^{-1}$), the largest residuals occur near line centers. These errors might be associated with the use of a Voigt line shape in the O_2 A-band absorption coefficient calculations rather than a more appropriate, collision-narrowed line shape. Ritter and Wilkerson (1987) found that line parameters derived using the Galatry line shapes reduced the residuals in laboratory measurements by up to a factor of 10 when compared to those obtained using the Voigt line shape. Beyond $13\,050\,cm^{-1}$, where the lines become progressively more saturated, the largest residuals are in the near wings and just beyond the band head. These residuals are likely to be due to subtle errors in the line mixing formulation adopted here (Tran and Hartmann, 2008). We do not yet have self-consistent estimates of line parameters (positions, strengths, widths, and pressure shifts) and line mixing coupling matrices for absorption lines that include collisional-narrowing as well as Doppler and

AMTD
5, 1–60, 2012

collisional broadening effects. This work is proceeding rapidly and new absorption coefficients will be implemented as they become available.

The similarity of the persistent A-band residuals in the GOSAT and TCCON fits has interesting implications for the other known sources of error in the GOSAT retrievals. These include the non-linearity in the TANSO-FTS Band-1 (Suto et al., 2011), the neglect of chlolorphyll fluorescence (Frankenberg et al., 2011b), and the use of radiance correction factors contaminated by atmospheric absorption. These factors may contribute to the observed scatter in the X_{CO_2} retrievals, but are not currently the most important sources of bias or persistent spectral residuals.

5.3 Minimizing the impact of systematic spectroscopic residuals: empirical noise

To reduce the impact of systematic, spectrally-dependent residuals (Fig. 4) on the evaluation of the cost function, χ^2 (c.f. Connor et al., 2008; O'Dell et al., 2011) in the ACOS GOSAT B2.8 X_{CO_2} product, the amplitude of the true noise was modified by introducing an "empirical noise" in each sounding, used in the measurement error covariance matrix, S_ε. The amplitude of the empirical noise in each SWIR spectral band was derived by examining all soundings over land from July 2009 that converged and passed the cloud screen filter and all other quality filters. For each sounding, the relative root-mean-square of the residuals in each band was defined by:

$$\mathrm{RRMS}_b = (\Sigma[y_{s,b,i} - y_{o,b,i}]^2/N_b)^{1/2}/S_b, \quad (1)$$

where $y_{s,b,i}$ and $y_{o,b,i}$ are the simulated and observed radiances at spectral point, i, in band, b, N_b is the number of spectral samples in band, b, S_b is the mean continuum signal level in band, b, and the summation extends over all spectral samples in the band.

By this definition, residuals due to instrument noise alone should yield values equal to the inverse of the instrument SNR, so that $\mathrm{RRMS}_b = \sigma_b/S_b$, where σ_b is the true noise in the band. For that case, RRMS should approach zero in the limit of high SNR.

AMTD
5, 1–60, 2012

This was not true for the July 2009 retrievals examined here. Figure 7 shows RRMS for each SWIR band as a function of 1/SNR. The RRMS values fall along a line, but each line has a significant offset from zero in the limit of large SNR. To account for this offset, we define an empirical noise in each sounding as:

$$\sigma'_{b,i} = A_b S_b + B_b \sigma_{b,i}, \quad (2)$$

where $\sigma_{b,i}$ is the estimated true instrument noise in spectral sample, i in band, b. The value of $\sigma_{b,i}$ is determined directly from each TANSO-FTS spectrum, at wavelengths just outside the spectral range used in the X_{CO_2} retrievals. The coefficients, A_b and B_b , were derived by fitting the RRMS values shown in Fig. 7 (Table 3). These values depend on the specific gas absorption cross sections and solar models used and are likely to change in the future as these input data evolve.

6 Developing post-processing filters and a sounding quality flag

As noted above, the accuracy of the ACOS X_{CO_2} retrievals can be compromised by low SNR, low surface reflectivity, large aerosol optical depths, as well as other factors. A post-screening process was developed to identify soundings with these characteristics so that they can be excluded from use in flux inversion models and other applications. While the B2.8 product includes all converged soundings that have passed the cloud screen, the data quality for each sounding is specified by a "Sounding Quality Flag". For the data presented here, retrievals are classified as "Good" only if they satisfy the criteria listed in column 2 of Table 4. Those classified into the "Caution" category must satisfy all of the criteria for "Good" spectra, except for the "X_{CO_2} a posteriori Error" and "Number of diverging steps." These criteria differ somewhat from those used in the simulations reported by Wunch et al. (2011) and O'Dell et al. (2011).

These criteria were derived using an approach similar to that used by Wunch et al. (2011). We assumed that the true X_{CO_2} was spatially invariant between 20° S and 70° S, and increasing in time with a secular increase of 1.89 ppm yr^{-1} (Fig. 8a).

AMTD
5, 1–60, 2012

We define ΔXCO_2 as the difference between the retrieved X_{CO_2} and its assumed true value; the mean bias of X_{CO_2} has been removed. The remaining panels in Fig. 8 show ΔXCO_2 as a function of each of the screening parameters in Table 4 (with the exception of the Cloud Flag, which is set prior to the retrieval process). A histogram showing the relative distribution of each retrieved parameter in this data set is also shown in each panel.

Figure 8b shows the dependence of ΔXCO_2 on the number of diverging steps in the retrieval. Ideally, even if the retrieval diverges in one or more steps, it should produce bias-free results if it eventually finds the true minimum in the cost function. However, this is rarely the case. Retrieval iterations that take any diverging steps exhibit both strong bias and more scatter than monotonically converging iterations. The ACOS/OCO-2 B2.8 post-processing screening process therefore rejects all retrievals with any diverging steps.

Figure 8c–e shows how ΔXCO_2 varies as the goodness of fit in SWIR bands 1, 2, and 3, measured by the reduced χ^2. Both the bias and standard deviation increase with increasing χ^2. For B2.8, all soundings with $\chi^2 > 1.2$ in any band are rejected. Figure 8f shows ΔXCO_2 as a function of the a posteriori uncertainty, σ_{XCO_2}. In practice, very few soundings with no diverging steps and $\chi^2 < 1.2$ have large a posteriori uncertainties, but those that do have anomalously high scatter. The a postiori X_{CO_2} error, σ_{XCO_2}, is largely driven by the SNR in the CO_2 bands, such that soundings with low signal levels have high values of σ_{XCO_2}. Hence, we require $\sigma_{XCO_2} < 1.5$ ppm for this quality flag in B2.8.

Retrievals of synthetic data show that there is a significant correlation between ΔX_{CO_2} and the difference between the a priori (ECMWF) surface pressure and the retrieved surface pressure, ΔP_{surf}. O'Dell et al. (2011) also see this behavior in retrievals of simulated data, suggesting that this is a fundamental property of the ACOS/OCO-2 retrieval approach. It is likely to be a manifestation of correlations between the Jacobians used in retrievals of surface pressure and CO_2. In addition, simulations using realistic cloud distributions and the cloud screening method adopted here indicate that

AMTD
5, 1–60, 2012

large values of ΔP_{surf} may result if clouds are missed by the cloud screening algorithm. Here, we require soundings to have $0 < \Delta P_{surf} < 20$ hPa to minimize biases and reduce the scatter associated with these processes (Fig. 8g). Finally, we find that both bias and scatter increase with increasing retrieved cloud and aerosol optical depth (AOD at 755 nm, Fig. 8h). B2.8 screens out all soundings with a retrieved AOD > 0.15.

The impact of the pre- and post-processing screens on the spatial coverage over land for July 2009 is shown in Fig. 9, which compares maps of the number of sounding in the complete data set, the number of soundings that pass the cloud and latitude filters, and those that pass all of the post-screening filters (Table 4). Optically-thick clouds reduce the coverage most over the tropics and in the upper mid-latitudes. Thinner clouds and aerosols, with optical depths too low to be caught by the cloud filter, but greater than 0.15, reduce the coverage far more in these regions, eliminating virtually all soundings over eastern North America, the Amazon, and southern Asia. Overall, these patterns are consistent with monthly mean values of cloud fraction from MODIS, which show persistent cloudiness in these regions during July 2009.

The requirement that $\chi^2 < 1.2$ in all bands has its largest impact on soundings acquired at high northerly latitudes during northern winter, where the surface is often covered by snow and ice. X_{CO_2} retrievals from soundings acquired over these surfaces often have large biases. These surfaces have a low reflectivity in the 1.61 and 2.06 µm bands, such that scattering by thin clouds and aerosols can constitute a large fraction of the total signal and can introduce significant uncertainties in the optical path lengths.

The performance of each step in the post-processing data screening process and its impact on the total yield of GOSAT soundings over land for July 2009 is illustrated in Fig. 10. The screens are applied in the sequence shown, such that soundings are rejected by the first screen that they fail, and are not considered by the subsequent screening steps. For July 2009, ~36 % of all soundings over land passed the cloud screen. The O_2 A-band χ^2 post-procesing filter rejects 23 % of these soundings. If this filter were eliminated, most of those soundings would be rejected by one of the two CO_2 χ^2 filters or by the diverging steps filter. In this set, less than 30 % of the

AMTD
5, 1–60, 2012

cloud-free soundings pass all of the screens. The total yield of the pre- and post-screening filters for July 2009 is therefore ~11 %. This is a relatively high yield when compared to the average return for the full 2-yr data set presented here (~7 %). It is also substantially larger than the ~3 % monthly-mean fraction of usable soundings reported for the standard GOSAT X_{CO_2} product (Yoshida et al., 2011).

7 Monthly maps of X_{CO_2} from B2.8

Figure 11 shows monthly maps of the X_{CO_2} retrievals over land collected between 4 April 2009 and 19 April 2011. The soundings plotted here have passed all of the pre- and post-screening criteria (Table 4). Only soundings over land are shown because the accuracy of the glint soundings over the ocean is still under investigation. The spatial coverage obtained during each month is limited to solar zenith angles <85°, and therefore varies with season. The low yields over high northern latitudes during northern winter are driven by a combination of factors. The sun is low, clouds are more prevalent, and large areas of the continents are covered by snow and ice, which have very low reflectances in the CO_2 bands, yielding very low SNR. Persistent cloudiness also reduces the yield of useful retrievals in the vicinity of the Inter Tropical Convergence Zone (ITCZ) and over much of southern Asia during the summer monsoon. Finally, the spatial resolution over land decreases somewhat after August 2010 when the TANSO-FTS cross-track sampling mode was changed to sample 3 cross-track points instead of 5.

For the data set shown in Fig. 11, the solar zenith angle limits and cloud screen eliminated ~58 % of all soundings over land. The post-processing screening criteria then removed ~83 % of the remaining soundings, reducing the end-to-end yield to less than 7 % of all soundings collected over land. Even with these relatively low yields, these results clearly illustrate the seasonal cycle of CO_2, with a strong draw-down in the Northern Hemisphere during the summer and subsequent build-up during the fall and winter months, with peak-to-peak amplitude between 8 and 12 ppm. Much less

AMTD
5, 1–60, 2012

variation is seen in the Southern Hemisphere, as expected. Consistent spatial patterns are seen from year-to-year, superimposed on the ~1.5 to 2 ppm yr^{-1} increase in X_{CO_2}.

If the ~7 ppm bias between the ACOS GOSAT and TCCON retrievals is spatially invariant, it should be possible to dramatically improve the agreement between these data sets by simply dividing each ACOS GOSAT X_{CO_2} estimate by ~0.982. Figure 12 shows that this approach substantially improves the agreement between the space-based ACOS/GOSAT retrievals and the TCCON results at latitudes between 45° S to 53° N for July 2009. However, this simple, ad hoc global offset reveals a small (1 to 2 ppm) north-south gradient, with too little X_{CO_2} at northern mid-latitudes, or too much at southern mid-latitudes, when compared to the available TCCON data. Comparisons for other months indicate that this residual bias changes over time. In addition, this simple offset correction does not reduce the scatter in the data within each latitude bin. These artifacts could still introduce spurious fluxes in source-sink inversion studies, compromising the value of these data.

To quantify these biases and gain greater insight into their origin, Wunch et al. (2011) compare ACOS GOSAT X_{CO_2} retrievals to TCCON results collected at mid-latitudes in the Southern Hemisphere (25° S to 55° S), where spatial and temporal variations in X_{CO_2} are known to be small (Pearman and Hyson, 1986; GLOBALVIEW CO_2, 2006, 2011; Wofsy et al., 2011). Observations collected at the Wollongong (34.4° S) and Lauder (45.0° S) TCCON stations were combined with GLOBALVIEW data to define the X_{CO_2} baseline, and remove a 1.89 ppm yr^{-1} trend and the small (<1 ppm) seasonal cycle between 25° S and 55° S. They then assume that all remaining differences between the ACOS GOSAT B2.8 product and this baseline were spurious, and searched for empirical correlations between these differences and observation or state properties.

In their tests, Wunch et al. (2011) start with the B2.8 X_{CO_2} retrievals shown at latitudes between 25° S and 55° S in Fig. 11. They divide the X_{CO_2} values by 0.982 to remove the global bias, and then apply two additional filters. The first eliminates all soundings collected using Gain M, because the accuracy of the TANSO-FTS spectra

AMTD
5, 1–60, 2012

is compromised by the micro-vibration problem identified above, and because the X_{CO_2} retrievals from these soundings are biased ~1 % higher than those obtained using Gain H. They then apply a second filter that eliminates most, if not all, observations over snow and ice covered surfaces, where the ACOS GOSAT retrieval algorithm yields anomalously low values of X_{CO_2}. This "blended albedo" filter was implemented by comparing the albedos retrieved in the O_2 A-band (A_{ABO2}) with those retrieved in the strong CO_2 band (A_{SCO2}). Soundings were retained only if their blended albedo satisfied the relationship: blended albedo $\equiv 2.4\, A_{AO2} - 1.13\, A_{SCO2} < 1$.

Even after applying these additional screening criteria, they find that differences between the retrieved X_{CO_2} and the ambient background between 25° S and 55° S show significant correlations with the blended albedo, surface pressure offset from the ECMWF prior, air mass, and the A-band signal levels. Wunch et al., derive a linear regression relationship to eliminate these biases. They show that this empirical approach substantially improves the agreement between ACOS-GOSAT and TCCON retrievals over the full range of latitudes sampled by TCCON stations (80° N to 45° S).

Here, we have used this regression formula to correct the X_{CO_2} soundings collected over land in July 2009 (Fig. 13). The fit to the TCCON results from the Lauder and Wollongong stations is not quite as good as that achieved in Wunch et al. (2011) because the data set used here includes the Gain M soundings over central Australia, which were excluded in their analysis. Even with this additional source of bias, this correction reduces the scatter slightly at most latitudes.

The impact of these empirical corrections on the spatial variations in X_{CO_2} is shown in Fig. 13b and c. At most latitudes, the global, 7 ppm bias (light brown shades in Fig. 13c) dominates the differences. Superimposed on this correction, the empirical regression relation reduces the X_{CO_2} estimates in the Amazon and in upper mid-latitudes (Russia, Mongolia, and Canada) by up to 3 ppm. The largest increases in X_{CO_2} are seen in Patagonia, where the large solar zenith angles and the presence of snow and ice on the ground during this season contribute large, positive air mass and "blended albedo" corrections.

AMTD
5, 1–60, 2012

One limitation of empirical corrections like those developed by Wunch et al. (2011) is that their validity can only be established in regions that are well sampled by other measurement techniques. While the reduced X_{CO_2} amounts in the northern mid-latitudes agree well with TCCON results collected at the Park Falls and Bialystok stations (see Fig. 10 of Wunch et al., 2011), Patagonia is poorly sampled by TCCON stations or other measurements, precluding direct validation of the positive X_{CO_2} adjustment in this region.

A substantial amount of progress has been made in identifying the root causes of many of the spurious correlations identified by Wunch et al. (2011). For example, as noted above, about half of the 7 ppm global bias in X_{CO_2} has been attributed to an underestimate of the O_2 A-band absorption cross sections. This problem can be resolved as soon as we have new estimates of the O_2 absorption cross sections that provide a self-consistent treatment of line parameters and line mixing coupling matrices for collision-narrowed lines. Meanwhile, we have begun to assess the impact of the approach proposed by Butz et al. (2011), which simply scales the O_2 A-band absorption coefficients to account for this air mass bias. We found that multiplying the existing O_2 A-band coefficients by 1.025, reduces the global surface pressure bias to near zero (Fig. 14). As expected, this change increases the retrieved X_{CO_2} values by ~4 ppm, eliminating about half of the bias between the ACOS GOSAT and TCCON results.

Much of the remaining global bias can be attributed to a recently discovered error in the ACOS implementation of the TANSO-FTS instrument model. The instrument line shape (ILS) in each spectral band is defined at several wavelengths throughout its spectral range. The ACOS/OCO-2 B2.8 algorithm included an option for interpolating the ILS linearly between these points, but this option was inadvertently disabled, such that the ILS varied as a step function at each point where it was specified. Recent tests indicate that this ILS interpolation error contributes a ~0.7 % (2.8 ppm) underestimate of the X_{CO_2} in the B2.8 ACOS GOSAT data product (Fig. 15). This error has been corrected in B2.9.

AMTD
5, 1–60, 2012

Other tests have provided insight into many of the spatially varying biases identified by Wunch et al. (2011). O'Dell et al. (2011) find that the spurious correlations with the "blended albedo" result from a fundamental limitation of the ACOS GOSAT algorithm's ability to discriminate optical path length contributions from thin, low clouds and aerosols, especially over ice-covered surfaces, which are quite dark at the wavelengths sampled by the CO_2 bands. Currently, the only option is to screen out all soundings with very low retrieved albedos in the 2.06 µm (SCO2) band. This approach is not ideal because it substantially reduces the yield, especially at high latitudes in the winter hemisphere, and may introduce additional sampling bias in the X_{CO_2} product.

Some of the scatter in the X_{CO_2} values may be associated with the recently discovered non-linear response of the O_2 A-band band (Band 1) of the TANSO-FTS (Suto et al., 2011). This calibration artifact was discovered during the course of a parallel investigation of chlorophyll fluorescence (Frankenberg et al., 2011a, b), which revealed an intensity dependence in the depth of solar Fraunhofer lines over Antarctica, where no fluorescence was expected. The JAXA GOSAT instrument team has since used the TANSO-FTS engineering model to investigate this issue and has recently traced its root cause to specific components in the detector signal chain and analog-to-digital converters (H. Suto, personal communication, 2011). These components apparently produce a non-linear response to the incident radiance at both low and high signal levels. Once the interferograms are Fourier transformed to produce spectra, these nonlinearities are manifested as a wavelength- and intensity-dependent zero level offset as well as more subtle changes in the instrument line shape. The GOSAT instrument team is currently collaborating with the ACOS and NIES algorithm teams to develop and validate a correction for these effects on the flight instrument. A revised version of GOSAT Level 1B product that corrects this problem is expected in the near future.

Butz et al. (2011) found that retrieving an intensity-dependent, wavelength-independent, zero-level offset for each sounding could substantially reduce the impact of instrument nonlinearity. This approach has been incorporated into B2.9 of the ACOS GOSAT algorithm along with the scaled O_2 A-band absorption coefficients and the ILS

AMTD
5, 1–60, 2012

implementation correction described above. Comparisons of preliminary B2.9 products and TCCON results for July 2009 are shown in Fig. 16. These changes eliminate the global bias and reduce scatter at all latitudes.

Spatial variations in prelimiary B2.9 X_{CO_2} products for July 2009 are shown in Fig. 17a. The B2.8 post-processing filters were used here to facilitate comparisons with the B2.8 results. The post-processing filters for B2.9 are currently being re-optimized to improve the quality and yield of this product. Differences between the B2.9 product and two different versions of the B2.8 product are shown in Fig. 17b and c. In Fig. 17b, the B2.8 product has been divided by 0.982 to remove the ~7 ppm X_{CO_2} bias, and then subtracted from the B2.9 product. In Fig. 17c, the B2.8 results were first corrected with the empirical approach developed by Wunch et al. (2011; "B2.8corrected") then subtracted from the B2.9 product. In general, differences between the B2.9 product and the B2.8corrected product are smaller than those with the B2.8offset product everywhere, suggesting that the overall bias has been reduced slightly. To quantify these changes, the empirical bias correction methods described by Wunch et al. (2011) have also been applied to preliminary versions of the B2.9 product. Comparisons of differences between raw and bias-corrected values for B2.8 (Fig. 13c) and B2.9 (Fig. 17d) show that spatial distribution of bias has not changed substantially, but the amplitude of the bias has been reduced by up to a factor of two in the B2.9 product.

Some of the largest differences between the B2.9 and both of the modified B2.8 products are seen over the bright surfaces of the Sahara desert and central Australia, where Gain M was used (Fig. b, c). In general, the bias between Gain-M and Gain-H soundings increased in the B2.9 product. The cause for these differences is not yet understood. This anomaly may require that all Gain M data be flagged as either "bad" or "caution" in the B2.9 product.

The next largest systematic differences between the B2.8 offset and the B2.9 results are once again seen in high northern mid-latitudes, the tropics, and in Patagonia. Interestingly, B2.9 produces values that are 1–2 ppm higher than those seen in B2.8offset, and 1–2 ppm lower than those produced by B2.8-corrected. As noted earlier, it is

AMTD
5, 1–60, 2012

currently not possible to validate the ACOS GOSAT retrievals of X_{CO_2} for these geographic regions due to the lack of TCCON data or other reliable measurements.

8 Discussion

The primary objective of the GOSAT mission is to return space-based observations of atmospheric CO_2 and CH_4 with relative accuracies of 1 % (~4 ppm) at sub-continental (1000 km by 1000 km) scales at 3-month intervals (Hamazaki et al., 2005; Nakajima et al., 2010). The results presented above indicate that once corrected for a global ~7 ppm bias, the B2.8 results yield typical standard deviations less than 3 ppm in 10° wide latitude bands at all but the highest latitudes. A preliminary analysis of the B2.9 product indicates that the standard deviations have been further reduced by up to 30 %. The regional scale biases in these data can be reduced further by applying empirical corrections, like those proposed by Wunch et al. (2011). We strongly recommend that an empirical correction of this kind be applied to the B2.8 product before it is used in carbon source-sink inversion studies, to minimize spurious fluxes associated with known biases in the retrieved X_{CO_2} estimates.

The global, 7 ppm X_{CO_2} bias has been largely eliminated and several other issues have been corrected in the B2.9 product. However, preliminary regression experiments like those described by Wunch et al. (2011) still show systematic, regional-scale biases similar to, but generally smaller than those seen in the B2.8 product. Ongoing improvements in the instrument calibration and O_2 A-band and CO_2 absorption coefficients are expected to reduce these biases in future ACOS GOSAT products, perhaps eventually yielding results with accuracies as high as 1 ppm over much of the sunlit hemisphere.

While we have made progress in improving the accuracy of the X_{CO_2} retrievals at sub-continental scales, substantial improvements in the overall yield and, more importantly, latitude coverage, will be needed before these space based measurements can reach their full potential. The ACOS B2.9 product addresses this objective to some extent by providing retrievals of GOSAT glint soundings over the ocean with error characteristics

AMTD
5, 1–60, 2012

similar to those of the standard products collected over land. More significant improvements in the retrieval algorithm and screening techniques will be needed to increase the range of solar zenith angles, especially over ice covered surfaces. Increasing the yields in persistently cloudy regions over the tropics or at high latitudes in the winter hemisphere may be even more challenging, given the relatively large footprint of the GOSAT TANSO-FTS.

9 Conclusions

GOSAT TANSO-FTS data have provided an invaluable resource for testing the ACOS/OCO-2 X_{CO_2} retrieval algorithm. Retrievals of X_{CO_2} from simulated data can yield insight into the information content of high resolution SWIR spectra acquired from space, as well as systematic biases in X_{CO_2} introduced by the retrieval approach (Connor et al., 2008; Bösch et al., 2011; O'Dell et al., 2011). However, even double-blind tests that employ different forward models for simulating observations and performing X_{CO_2} retrievals cannot account for uncertainties that are common to both forward models, or otherwise difficult to model. These factors include common gas absorption coefficients, top-of-atmosphere solar spectra, aerosol optical properties, and unidentified uncertainties in instrument radiometric, spectroscopic, or geometric performance. The GOSAT data have provided valuable insights into all of these areas, as well as the impact of interactions between these sources of uncertainty on X_{CO_2}. Foremost among these are the uncertainties in the O_2 A-band cross-sections, which account for roughly half of the global, 7 ppm bias in the ACOS GOSAT X_{CO_2} retrievals.

The availability of GOSAT data has also provided opportunities to refine the vicarious calibration and validation approaches planned for the OCO-2 mission. The basic approach for ground-based vicarious calibration of space-based radiometers is well established (c.f. Thome et al., 2001; Bruegge et al., 2002), but the GOSAT Railroad Valley campaigns provided an opportunity to refine these techniques for application to a high-resolution SWIR spectrometer. Results derived from these experiments have played a

AMTD
5, 1–60, 2012

significant role in the diagnosis and correction of the long-term drift in the throughput of the TANSO-FTS instrument, substantially reducing the associated ~1.5 ppm bias in the ACOS GOSAT X_{CO_2} product.

Finally, while TCCON has become a reliable source of high quality ground-based remote sensing measurements of X_{CO_2}, GOSAT provided the first opportunity to run an end-to-end test of the TCCON-based validation architecture developed for the OCO-2 mission. Detailed comparisons between X_{CO_2} retrievals from GOSAT and TCCON have helped to detect and quantify regional-scale biases in the ACOS GOSAT X_{CO_2} product. Comparisons of spectrally dependent residuals in fits to GOSAT and TCCON observations have also helped to diagnose the source of spectroscopic errors that contribute bias and scatter in the space-based retrievals of X_{CO_2}. These developments, combined with the improvements being implemented in the ACOS/OCO-2 retrieval algorithm, are expected to accelerate the delivery of high quality OCO-2 data products, once that satellite is successfully launched and inserted into orbit.

Acknowledgements. The GOSAT spectra were provided to the ACOS Team through a GOSAT Research Announcement (RA) agreement between the California Institute of Technology and the three parties, JAXA, NIES and the MOE. The meteorological data used to initialize the retrievals and as a reference for comparison with the surface pressure results were based on data and products of the European Centre for Medium-Range Weather Forecasts (ECMWF). TCCON data were obtained from the TCCON Data Archive, operated by the California Institute of Technology from the website at http://tccon.ipac.caltech.edu/. Part of the research described here was carried out at the Jet Propulsion Laboratory, California Institute of Technology, under a contract with the National Aeronautics and Space Administration.

References

Benner, D. C., Miller, C. E., and Devi, V. M.: Constrained multispectrum analysis of CO_2–Ar broadening at 6227 and 6348 cm^{-1}, Can. J. Phys., 87, 499–515, doi:10.1139/P09-014, 2009.

AMTD
5, 1–60, 2012

Benner, D. C., Devi, V. M., Nugent, E., Sung, D., Brown, L. R., Miller, C. E., and Toth, R. A.: Line parameters of carbon dioxide in the 4850 cm^{-1} region. The 22nd Colloquium on High Resolution Molecular Spectroscopy, N19, 262, 2011.

Bösch, H., Toon, G., Sen, B., Washenfelder, R., Wennberg, P., Buchwitz, M., De Beek, R., Burrows, J., Crisp, D., Christi, M., Connor, B. J., Natraj, V., and Yung, Y. L.: Space-based near-infrared CO_2 measurements: Testing the Orbiting Carbon Observatory retrieval algorithm and validation concept using SCIAMACHY observations over Park Falls, Wisconsin, J. Geophys. Res., 111, 0148–0227, 2006.

Bösch, H., Baker, D., Connor, B., Crisp, D., and Miller, C.: Global Characterization of CO_2 Column Retrievals from Shortwave-Infrared Satellite Observations of the Orbiting Carbon Observatory-2 Mission, Remote Sens., 3, 270–304, doi:10.3390/rs3020270, 2011.

Bruegge, C. J., Chrien, N. L., Ando, R. R., Diner, D. J., Abdou, W. A., Helmlinger, M. C., Pilorz, S. H., and Thome, K. J.: Early validation of the Multi-angle Imaging SpectroRadiometer (MISR) radiometric scale, IEEE T. Geosci. Remote, 40, 1477–1492, 2002.

Butz, A., Guerlet, S., Hasekamp, O., Schepers, D., Galli, A., Aben, I., Frankenberg, C., Hartmann, J.-M., Tran, H., Kuze, A., Keppel-Aleks, G., Toon, G., Wunch, D., Wennberg, P., Deutscher, N., Griffith, D., Macatangay, R., Messerschmidt, J., Notholt, J., and Warneke, T.: Toward accurate CO_2 and CH_4 observations from GOSAT, Geophys. Res. Lett., 38, L14812, doi:10.1029/2011GL047888, 2011.

Connor, B., Bösch, H., Toon, G., Sen, B., Miller, C., and Crisp, D.: Orbiting Carbon Observatory: Inverse method and prospective error analysis, J. Geophys. Res., 113, D05305, doi:10.1029/2006JD008336, 2008.

Conway, T. J., Lang, P. M., and Masarie, K. A.: Atmospheric Carbon Dioxide Dry Air Mole Fractions from the NOAA ESRL Carbon Cycle Cooperative Global Air Sampling Network, 1968–2010, Version: 2011-10-14, available at: ftp://ftp.cmdl.noaa.gov/ccg/co2/flask/event/, last access: December 2011, 2011.

Crisp, D., Atlas, R. M., Breon, F.-M., Brown, L. R., Burrows, J. P., Ciais, P., Connor, B. J., Doney, S. C., Fung, I. Y., Jacob, D. J., Miller, C. E., O'Brien, D., Pawson, S., Randerson, J. T., Rayner, P., Salawitch, R. J., Sander, S. P., Sen, B., Stephens, G. L., Tans, P. P., Toon G. C., Wennberg, P. O., Wofsy, S. C., Yung, Y. L., Kuang, Z., Chudasama, B., Sprague, G., Weiss, B., Pollock, R., Kenyon, D., and Schroll, S.: The Orbiting Carbon Observatory (OCO) Mission, Adv. Space. Res., 34, 700–709, 2004.

Crisp, D., Miller, C. E., and DeCola, P. L.: NASA Orbiting Carbon Observatory: measuring

AMTD
5, 1–60, 2012

the column averaged carbon dioxide mole fraction from space, J. Appl. Remote Sens., 2, 023508, doi:10.1117/1.2898457, 2008.

Crisp, D.: Opportunities for Coordinated Observations of CO_2 with the Orbiting Carbon Observatory (OCO) and Greenhouse Gases Observing Satellite (GOSAT), Trans. JSASS Space Tech. Japan, 7, 41–43, 2009.

Crisp, D., Bösch, H., Brown, L., Castano, R., Christi, M., Connor, B., Frankenberg, C., McDuffie, J., Miller, C. E., Natraj, V., O'Dell, C., O'Brien, D., Polonsky, I., Oyafuso, F., Thompson, D., Toon, G., and Spurr, R.: OCO (Orbiting Carbon Observatory)-2 Level 2 Full Physics Retrieval Algorithm Theoretical Basis, Tech. Rep. OCO D-65488, NASA Jet Propulsion Laboratory, California Institute of Technology, Pasadena, CA, version 1.0 Rev 4, available at: http://disc.sci.gsfc.nasa.gov/acdisc/documentation/ACOS.shtml, last access: December 2011, 2010.

Deutscher, N. M., Griffith, D. W. T., Bryant, G. W., Wennberg, P. O., Toon, G. C., Washenfelder, R. A., Keppel-Aleks, G., Wunch, D., Yavin, Y., Allen, N. T., Blavier, J.-F., Jiménez, R., Daube, B. C., Bright, A. V., Matross, D. M., Wofsy, S. C., and Park, S.: Total column CO_2 measurements at Darwin, Australia – site description and calibration against in situ aircraft profiles, Atmos. Meas. Tech., 3, 947–958, doi:10.5194/amt-3-947-2010, 2010.

Devi, V. M., Benner, D. C., Brown, L. R., Miller, C. E., and Toth, R. A.: Line mixing and speed dependence in CO_2 at 6227.9 cm^{-1}: Constrained multispectrum analysis of intensities and line shapes in the 30013 < – 00001 band, J. Mol. Spect., 245, 52–80, doi:10.1016/j.jms.2007.05.015, 2007.

Frankenberg, C., Butz, A., and Toon, G. C.: Disentangling chlorophyll fluorescence from atmospheric scattering effects in O_2 A-band spectra of reflected sun-light, Geophys. Res. Lett., 38, L03801, doi:10.1029/2010GL045896, 2011a.

Frankenberg, C., Fisher, J. B., Worden, J., Badgley, G., Saatchi, S. S., Lee, J.-E., Toon, G. C., Butz, A., Jung, M., Kuze, A., and Yokota, T.: New global observations of the terrestrial carbon cycle from GOSAT: Patterns of plant fluorescence with gross primary productivity, Geophys. Res. Lett., 38, L17706, doi:10.1029/2011GL048738, 2011b.

GLOBALVIEW-CO2: Cooperative Atmospheric Data Integration Project – Carbon Dioxide, CDROM, NOAA GMD, Boulder, Colorado, 2006.

GLOBALVIEW-CO2: Cooperative Atmospheric Data Integration Project – Carbon Dioxide, CD-ROM, NOAA ESRL, Boulder, Colorado, also available on Internet via anonymous FTP: ftp://ftp.cmdl.noaa.gov/ccg/co2/GLOBALVIEW/, last access: December 2011, 2011.

Hamazaki, T., Kaneko, Y., and Kuze, A.: Carbon Dioxide Monitoring from The Gosat Satellite,

AMTD
5, 1–60, 2012

Proc. Comm. VII, ISPRS, Istanbul, 225–227, 2004.
Hamazaki, T., Kaneko, Y., Kuze, A., and Kondo, K.: Fourier transform spectrometer for greenhouse gases observing satellite (GOSAT), in: Proc. SPIE, 5659, p. 73, doi:10.1117/12.581198, 2005.
Kahn, R., Banerjee, P., and McDonald, D.: Sensitivity of multiangle imaging to natural mixtures of aerosols over ocean, J. Geophys. Res., 106, 18219–18238, doi:10.1029/2000JD900497, 2001.
Kuang, Z. M., Margolis, J., Toon, G., Crisp, D., and Yung, Y. L.: Spaceborne Measurements of Atmospheric CO_2 by High-resolution NIR Spectrometry of Reflected Sunlight: An Introductory Study. Geophys. Res. Lett., 29, 1716, doi:10.1029/2001GL014298, 2002.
Kuze. A., Suto. H., Nakajima, M., and Hamazaki, T.: Thermal and near infrared sensor for carbon observation Fourier-transform spectrometer on the Greenhouse Gases Observing Satellite for greenhouse gases monitoring, Appl. Opt., 48, 6716–6733, doi:10.1364/AO.48.006716, 2009a.
Kuze. A., Suto, H., Shiomi, K., Nakajima, M., and Hamazaki, T.: On-orbit performance and level 1 data processing of TANSO-FTS and CAI on GOSAT, Sensors, Systems, and Next-Generation Satellites XIII, edited by Roland Meynart, Steven P. Neeck, Haruhisa Shimoda, Proc. SPIE, 7474, 74740I, doi:10.1117/12.830152, 2009b.
Kuze, A., O'Brien, D. M., Taylor, T. E., Day, J. O., O'Dell, C., Kataoka, F., Yoshida, M., Mitomi, Y., Bruegge, C., Pollock, H., Basilio, R., Helmlinger, M., Matsunaga, T., Kawakami, S., Shiomi, K., Urabe, T., and Suto, H.: Vicarious calibration of the GOSAT sensors using the Railroad Valley desert playa, IEEE T. Geosci. Remote, 49, 1781–1795, doi:10.1109/TGRS.2010.2089527, 2011.
Messerschmidt, J., Geibel, M. C., Blumenstock, T., Chen, H., Deutscher, N. M., Engel, A., Feist, D. G., Gerbig, C., Gisi, M., Hase, F., Katrynski, K., Kolle, O., Lavri, J. V., Notholt, J., Palm, M., Ramonet, M., Rettinger, M., Schmidt, M., Sussmann, R., Toon, G. C., Truong, F., Warneke, T., Wennberg, P. O., Wunch, D., and Xueref-Remy, I.: Calibration of TCCON column-averaged CO_2: the first aircraft campaign over European TCCON sites, Atmos. Chem. Phys., 11, 10765–10777, doi:10.5194/acp-11-10765-2011, 2011.
Miller, C. E., Crisp, D., DeCola, P. L., Olsen, S. C., Randerson, J. T., Michalak, A. M., Alkhaled, A., Rayner, P., Jacob, D. J., Suntharalingam, P., Jones, D. B. A., Denning, A. S., Nicholls, M. E., Doney, S. C., Pawson, S., Bösch, H., Connor, B. J., Fung, I. Y., O'Brien, D., Salawitch, R. J., Sander, S. P., Sen, B., Tans, P., Toon, G. C., Wennberg, P. O., Wofsy, S. C., Yung, Y. L.,

AMTD
5, 1–60, 2012

and Law, R. M.: Precision requirements for space-based X_{CO_2} data, J. Geophys. Res., 112, D10314, doi:10.1029/2006JD007659, 2007.
Nakajima, M., Kuze, A., Kawakami, S., Shiomi, K., adn Suto, H.: Monitoring of the greenhouse gases from space by GOSAT, International Archives of the Photogrammetry, Remote Sensing and Spatial Information Science, XXXVIII, Part 8, JAXA Special Session-5, 2010.
O'Brien, D. M. and Rayner, P. J.: Global observations of the carbon budget 2. CO_2 column from differential absorption of reflected sunlight in the 1.61 μm band of CO_2, J. Geophys. Res., 107, ACH6-1, doi:10.1029/2001JD000617, 2002.
O'Brien, D. M., Polonsky, I., Kuze, A., Kikuchi, N., and Natraj, V.: Validation of the polarization model for GOSAT, in preparation, 2011.
O'Dell, C. W., Connor, B., Bösch, H., O'Brien, D., Frankenberg, C., Castano, R., Christi, M., Crisp, D., Eldering, A., Fisher, B., Gunson, M., McDuffie, J., Miller, C. E., Natraj, V., Oyafuso, F., Polonsky, I., Smyth, M., Taylor, T., Toon, G. C., Wennberg, P. O., and Wunch, D.: The ACOS CO_2 retrieval algorithm - Part 1: Description and validation against synthetic observations, Atmos. Meas. Tech. Discuss., 4, 6097–6158, doi:10.5194/amtd-4-6097-2011, 2011.
Olsen, S. C. and Randersonk J. T.: Differences between surface and column atmospheric CO_2 and implications for carbon cycle research, J. Geophys. Res., 109, D02301, doi:10.1029/2003JD003968, 2004.
Rayner, P. J. and O'Brien, D. M.: The utility of remotely sensed CO_2 concentration data in surface source inversions, Geophys. Res. Lett., 28, 175–178, doi:10.1029/2000GL011912, 2001.
Pearman, G. I. and Hyson, P.: Global transport and inter-reservoir exchange of carbon dioxide with particular reference to stable isotopic distributions, J. Atmos. Chem, 4, 81–124, 1986.
Ritter, K. J. and T. D. Wilkerson: High-resolution spectroscopy of the oxygen A band, J. Mol. Spectrosc., 121, 1–19, 1987.
Rodgers, C.: Inverse methods for atmospheric sounding: Theory and practice, World Scientific Singapore, 2000.
Shiomi, K., Kawakami,S., Kina, T., Mitomi, Y., Yoshida, M., Sekio, N., Kataoka, F., and Higuchi, R.: GOSAT Level 1 processing and in-orbit calibration plan, Sensors, Systems, and Next-Generation Satellites XII, edited by: Meynart, R., Neeck, S. P., Shimoda, H., and Habib, S., Proc. SPIE, 7106, doi:10.1117/12.800278, 2008.
Suto, H., Kuze. A., Shiomi, K., Nakajima, M., and Hamazaki, T.: Updated Level-1 processing after two-years operation of TANSO-FTS, Proc. SPIE, 8154, 81541A, doi:10.1117/12.893405,

AMTD
5, 1–60, 2012

2011.
Taylor, T. E., O'Dell, C. W., O'Brien, D. M., Kikuchi, N., Yokota, T., Nakajima, T. Y., Ishida, H., Crisp, D., and Nakajima, T.: Comparison of cloud-screening methods applied to GOSAT near-infrared spectra, IEEE T. Geosci. Remote, 49, 1–15, doi:10.1109/TGRS.2011.2160270, 2011.
Thome, K., Smith, N., and Scott, K.: Vicarious calibration of MODIS using Railroad Valley Playa, in: Proc. IGARSS, 3, 1209–1211, 2001.
Toth, R. A., Brown L. R., Miller C. E., Devi V. M., and Benner D. C.: Line strengths of $^{12}C^{16}O_2$: 4550–7000 cm^{-1}, J. Mol. Spectrosc. 239, 221–242, 2006a.
Toth, R. A., Brown L. R., Miller C. E., Devi V. M., and Benner D. C.: Self-broadened widths and shifts of CO_2, J. Mol. Spectrosc., 239, 243–271, 2006b.
Toth, R. A., Miller, C. E., Brown, L. R., Devi, V. M., and Benner, D. C.: Line positions and strengths of $^{16}O^{12}C^{18}O$, $^{18}O^{12}C^{18}O$ and $^{17}O^{12}C^{18}O$ between 2200 and 7000 cm^{-1}, J. Mol. Spectrosc., 243, 43–61, 2007a.
Toth, R. A., Miller, C. E., Devi, V. M., Benner, D. C., and Brown, L. R.: Air-broadened width and pressure shift coefficients of $^{12}C^{16}O_2$: 4700–7000 cm^{-1}, J. Mol. Spectrosc., 246, 133–157, 2007b.
Toth, R. A., Miller, C. E., Brown, L. R., Devi, V. M., and Benner, D. C.: Line strengths of $^{16}O^{13}C^{16}O$, $^{16}O^{13}C^{18}O$, $^{16}O^{13}C^{17}O$ and $^{18}O^{13}C^{18}O$ between 2200 and 6800 cm^{-1}, J. Mol. Spectrosc. 251, 64–89, 2008a.
Toth, R. A., Brown L. R., Miller C. E., Devi V. M., and Benner D. C.: Spectroscopic database of CO_2 line parameters: 4300–7000 cm^{-1}, J. Quant. Spectrosc. Radiat., 109, 906–921, 2008b.
Washenfelder, R. A., Toon, G. C., Blavier, J.-F., Yang, Z., Allen, N. T., Wennberg, P. O., Vay, S. A., Matross, D. M., and Daube, B. C.: Carbon dioxide column abundances at the Wisconsin Tall Tower site, J. Geophys. Res., 111, D22305, doi:10.1029/2006JD007154, 2006.
Watanabe, H., Ishihara, H., Hayashi, K., Kawazoe, F., Kikuchi, N., Eguchi, N., Matsunaga, T., and Yokota, T.: Detailed Design of the GOSAT DHF at NIES and Data Acquisition/Processing/Distribution Strategy, Sensors, Systems, and Next-Generation Satellites XII, edited by: Meynart, R., Neeck, S. P., Shimoda, H., and Habib, S., Proc. SPIE, 7106, 71060N, doi:10.1117/12.801238, 2008.
Watanabe, H., Yuki, A., Hayashi, K., Kawazoe, F., Kikuchi, N., Takahashi, F., Matsunaga, T., and Yokota, T.: GOSAT higher level product status 1.5 year after the launch, Proc. SPIE, 7826, 782606, doi:10.1117/12.898391, 2010.

AMTD
5, 1–60, 2012

Wofsy, S. C., Daube, B. C., Jimenez, R., Kort, E., Pittman, J. V., Park, S., Commane, R., Xiang, B., Santoni, G., Jacob, D., Fisher, J., Pickett-Heaps, C., Wang, H., Wecht, K., Wang, Q.- Q., Stephens, B. B., Schertz, S., Romashkin, P., Campos, T., Haggerty, J., Cooper, W. A., Rogers, D., Beaton, S., Elkins, J. W., Fahey, D., Gao, R., Moore, F., Montzka, S. A., Schwartz, J. P., Hurst, D., Miller, B., Sweeney, C., Oltmans, S., Nance, D., Hintsa, E., Dutton, G., Watts, L. A., Spackman, R., Rosenlof, K., Ray, E., Zondlo, M., Diao, M., Mahoney, M. J., Chahine, M., Olsen, E., Keeling, R., Bent, J., Atlas, E. A., Lueb, R., Patra, P., Ishijima, K., Engelen, R., Nassar, R., Jones, D. B., and Mikaloff-Fletcher, S.: HIAPER Pole-to-Pole Observations (HIPPO): Fine grained, global scale measurements for determining rates for transport, surface emissions, and removal of climatically important atmospheric gases and aerosols, Phil. Trans. Roy. Soc. A, 369, 2073–2086, doi:10.1098/rsta.2010.0313, 2011.

Wunch, D., Toon, G. C., Wennberg, P. O., Wofsy, S. C., Stephens, B. B., Fischer, M. L., Uchino, O., Abshire, J. B., Bernath, P., Biraud, S. C., Blavier, J.-F. L., Boone, C., Bowman, K. P., Browell, E. V., Campos, T., Connor, B. J., Daube, B. C., Deutscher, N. M., Diao, M., Elkins, J. W., Gerbig, C., Gottlieb, E., Griffith, D. W. T., Hurst, D. F., Jiménez, R., Keppel-Aleks, G., Kort, E. A., Macatangay, R., Machida, T., Matsueda, H., Moore, F., Morino, I., Park, S., Robinson, J., Roehl, C. M., Sawa, Y., Sherlock, V., Sweeney, C., Tanaka, T., and Zondlo, M. A.: Calibration of the Total Carbon Column Observing Network using aircraft profile data, Atmos. Meas. Tech., 3, 1351–1362, doi:10.5194/amt-3-1351-2010, 2010.

Wunch, D., Toon, G. C., Blavier, J.-F. L., Washenfelder, R., Notholt, J., Connor, B. J., Griffith, D. W. T., Sherlock, V., and Wennberg, P. O.: The Total Carbon Column Observing Network, Phil. Trans. Roy. Soc. A, 369, 2087–2112, doi:10.1098/rsta.2010.0240, 2011a.

Wunch, D., Wennberg, P. O., Toon, G. C., Connor, B. J., Fisher, B., Osterman, G. B., Frankenberg, C., Mandrake, L., O'Dell, C., Ahonen, P., Biraud, S. C., Castano, R., Cressie, N., Crisp, D., Deutscher, N. M., Eldering, A., Fisher, M. L., Griffith, D. W. T., Gunson, M., Heikkinen, P., Keppel-Aleks, G., Kyrö, E., Lindenmaier, R., Macatangay, R., Mendonca, J., Messerschmidt, J., Miller, C. E., Morino, I., Notholt, J., Oyafuso, F. A., Rettinger, M., Robinson, J., Roehl, C. M., Salawitch, R. J., Sherlock, V., Strong, K., Sussmann, R., Tanaka, T., Thompson, D. R., Uchino, O., Warneke, T., and Wofsy, S. C.: A method for evaluating bias in global measurements of CO_2 total columns from space, Atmos. Chem. Phys., 11, 12317–12337, doi:10.5194/acp-11-12317-2011, 2011b.

Yokota, T., Oguma, H., Morino, I., Higurashi, A., Aoki, T., and Inoue, G.: Test measurements by a BBM of the nadir-looking SWIR FTS aboard GOSAT to monitor CO_2 column density from

AMTD
5, 1–60, 2012

space, Proc. SPIE, 5652, 182, doi:10.1117/12.578497, 2004.

Yokota, T., Yoshida, Y., Eguchi, N., Ota, Y., Tanaka, T., Watanabe, H., and Maksyutov, S.: Global Concentrations of CO_2 and CH_4 Retrieved from GOSAT: First Preliminary Results, SOLA – Scientific Online Letters on the Atmosphere, 5, 160–163, 2009.

Yoshida, Y., Ota, Y., Eguchi, N., Kikuchi, N., Nobuta, K., Tran, H., Morino, I., and Yokota, T.: Retrieval algorithm for CO_2 and CH_4 column abundances from short-wavelength infrared spectral observations by the Greenhouse Gases Observing Satellite, Atmos. Meas. Tech., 4, 717–734, doi:10.5194/amt-4-717-2011, 2011.

Table 1. GOSAT TANSO-FTS Spectral bands and ACOS/OCO-2 Spectral Ranges. The spectral resolution (full width at half maximum of the instrument line shape function) for the two polarizations, P and S, are specified separately (Kuze et al., 2009).

Band	Target Species	TANSO-FTS Spectral Range	Spectral Resolution	ACOS/OCO-2 Range Used	Band Name
1	O_2 A-band	12 900 to 13 200 cm^{-1} (0.758 to 0.775 μm)	1P 0.356 cm^{-1} 1S 0.367 cm^{-1}	12950 to 13190 cm^{-1} (0.758 to 0.772 μm)	ABO2
2	CO_2, CH_4	5800 to 6400 cm^{-1} (1.56 to 1.72 μm)	2P 0.258 cm^{-1} 2S 0.257 cm^{-1}	6166 to 6286 cm^{-1} (1.591 to 1.622 μm)	WCO2
3	CO_2	4800 to 5200 cm^{-1} (1.92 to 2.08 μm)	3P 0.262 cm^{-1} 3S 0.263 cm^{-1}	4810 to 4897 cm^{-1} (2.042 to 2.079 μm)	SCO2
4	H_2O, O_3, mid-tropospheric CO_2 and CH_4	700 to 1800 cm^{-1} (5.56 to 14.3 μm)	0.27 cm^{-1}	N/A	N/A

AMTD
5, 1–60, 2012

Table 2. Total Column Carbon Observing Network (TCCON) stations used in this study.

Station	Latitude	Longitude	Surface Elevation
Lauder, New Zealand	45.038° S	169.684° E	0.37 km
Wollongong, Australia	34.406° S	150.879° E	0.03 km
Darwin, Australia	12.424° S	130.892° E	0.03 km
Tsukuba, Japan	36.051° N	140.122° E	0.03 km
Lamont, OK, USA	36.604° N	−97.486° E	0.32 km
Park Falls, WI, USA	45.945° N	−90.237° E	0.44 km
Orleans, France	47.970° N	2.113° E	0.13 km
Bialystok, Poland	53.230° N	23.025° E	0.18 km

AMTD
5, 1–60, 2012

Table 3. Empirical Noise Coefficients.

Band	Name	A_b	B_b
1	O_2 A-band (ABO2)	0.002343	0.8969
2	Weak CO_2 Band (WCO2)	0.001658	0.8918
3	Strong CO_2 Band (SCO2)	0.002877	0.8795

AMTD
5, 1–60, 2012

Table 4. Retrieval Validity Criteria for B2.8.

Quantity	Good	Caution	Bad
Cloud Flag	0	0	1
Outcome	1 or 2	1 or 2	0
χ^2 O_2 A-band	< 1.2	< 1.2	≥ 1.2
χ^2 Weak CO_2	< 1.2	< 1.2	≥ 1.2
χ^2 Strong CO_2	< 1.2	< 1.2	≥ 1.2
Total Aerosol Optical Depth	< 0.15	< 0.15	≥ 0.15
Surface Pressure Difference	0 to 20 hPa	0 to 20 hPa	$< 0, \geq 20$ hPa
X_{CO_2} A Posteriori Error	< 1.5 ppm	≥ 1.5 ppm	≥ 1.5 ppm
Number of Diverging Steps	0	≥ 1	≥ 1

AMTD
5, 1–60, 2012

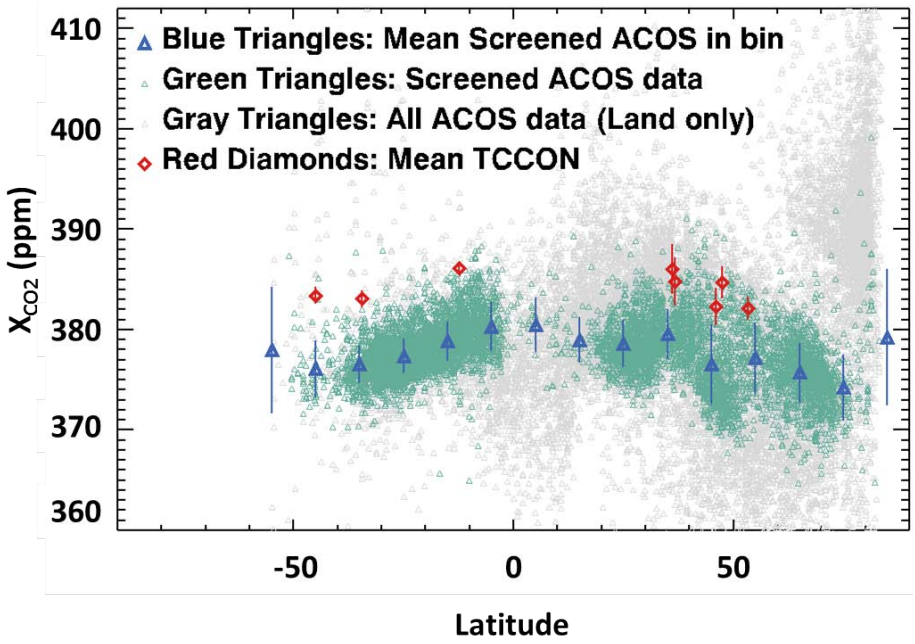

Fig. 1. All converged, cloud-free ACOS GOSAT B2.8 X_{CO_2} retrievals for soundings acquired over land at solar zenith angles < 85° during July 2009 (grey triangles) are compared to TCCON retrievals from that month (red diamonds). ACOS GOSAT soundings that also pass a series of post-processing filters (see text) are over-plotted as green triangles. These screened values have been averaged over 10° wide zonal bands to derive the zonal mean estimates of X_{CO_2} (blue triangles with 1-σ error bars). The TCCON results are from the stations listed in Table 2.

AMTD
5, 1–60, 2012

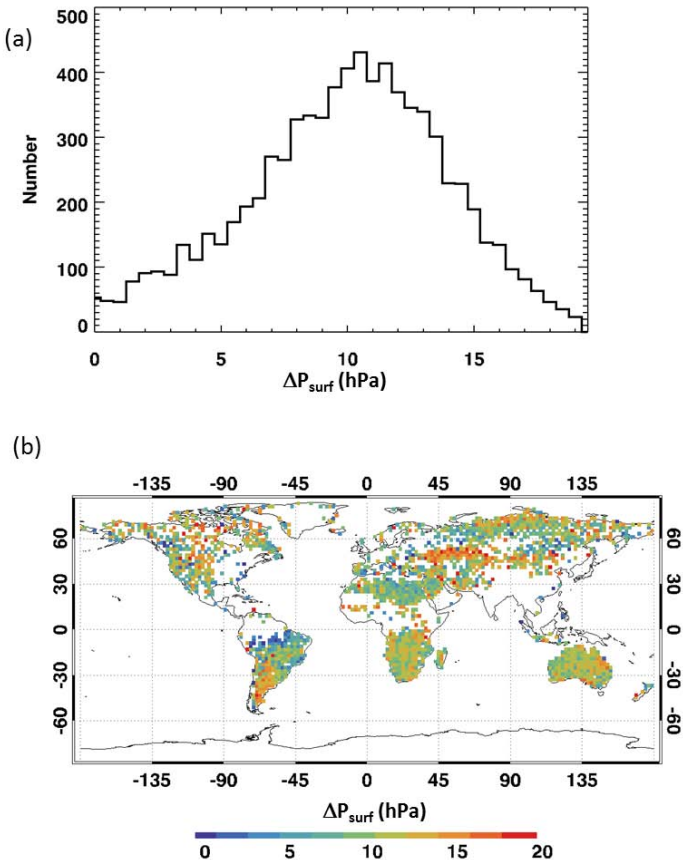

Fig. 2. **(a)** Histogram of differences between the retrieved surface pressures and the surface pressure prior estimated from ECMWF data, ΔP_{surf} (hPa), for all soundings over land in July 2009. **(b)** Map of differences between the retrieved surface pressure and the prior for July 2009.

AMTD
5, 1–60, 2012

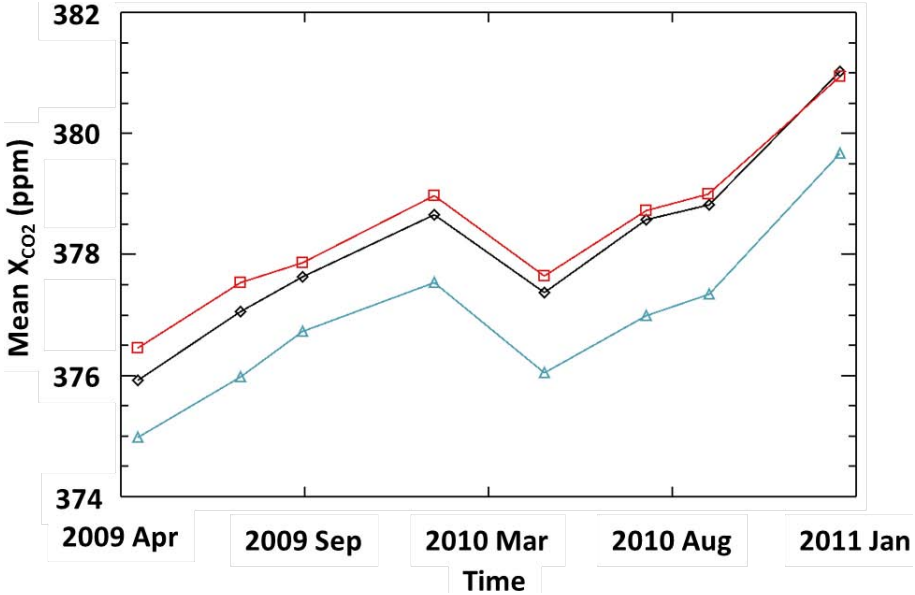

Fig. 3. Mean X_{CO_2} estimates over Australia are shown as a function of time for three different estimates of the time-dependent throughput of the TANSO-FTS. The blue curve shows X_{CO_2} retrievals assuming that the radiometric calibration coefficients derived from pre-launch tests did not change. A preliminary version of the time-dependent throughput correction was included in the B2.8 product (black line). A refined, time-dependent throughput correction that was developed more recently (red curve), produces an additional X_{CO_2} correction that decreases from ~0.5 ppm early in the GOSAT mission to slightly less than zero in early 2011.

AMTD
5, 1–60, 2012

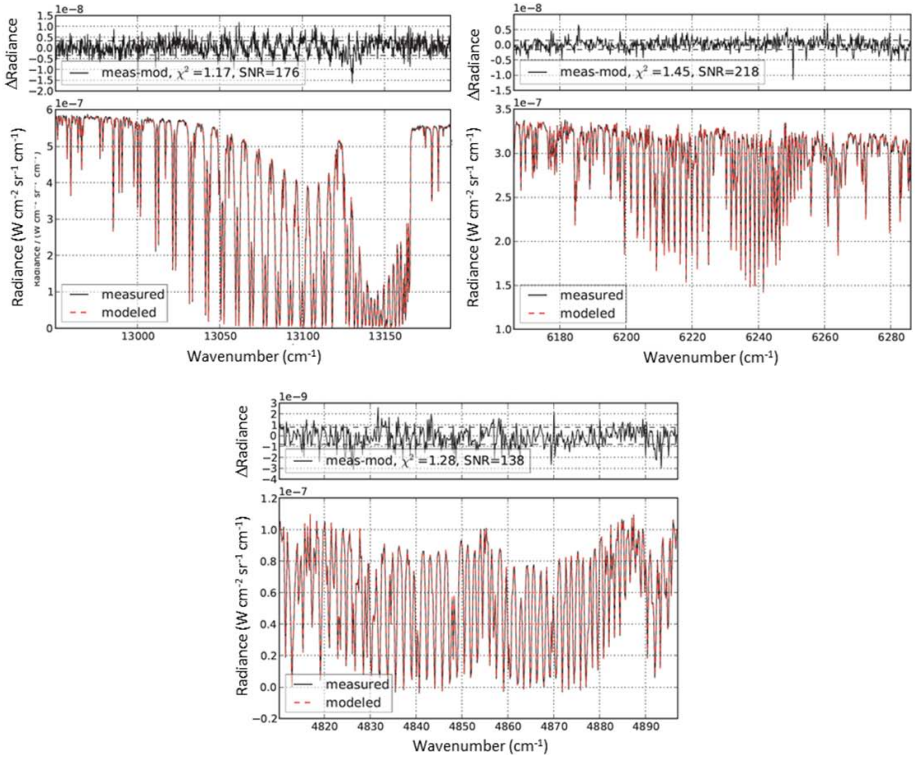

Fig. 4. Synthetic (red) and measured (black) spectra for a converged retrieval of a sounding acquired at 41.2° N, −95.8° E on 22 July 2010, just north of the Lamont Oklahoma TCCON station. This was a relatively bright sounding, collected at a solar zenith angle of 25.2° and an observation zenith 20.8°, yielding signal to noise ratios of 176, 218, and 138 in the ABO2, WCO2, and SCO2 bands, respectively. The retrieved X_{CO_2}, surface pressure, and aerosol optical depth at 0.755 µm for this sounding were 388.7 ppm, 975.8 hPa, and 0.11, respectively.

AMTD
5, 1–60, 2012

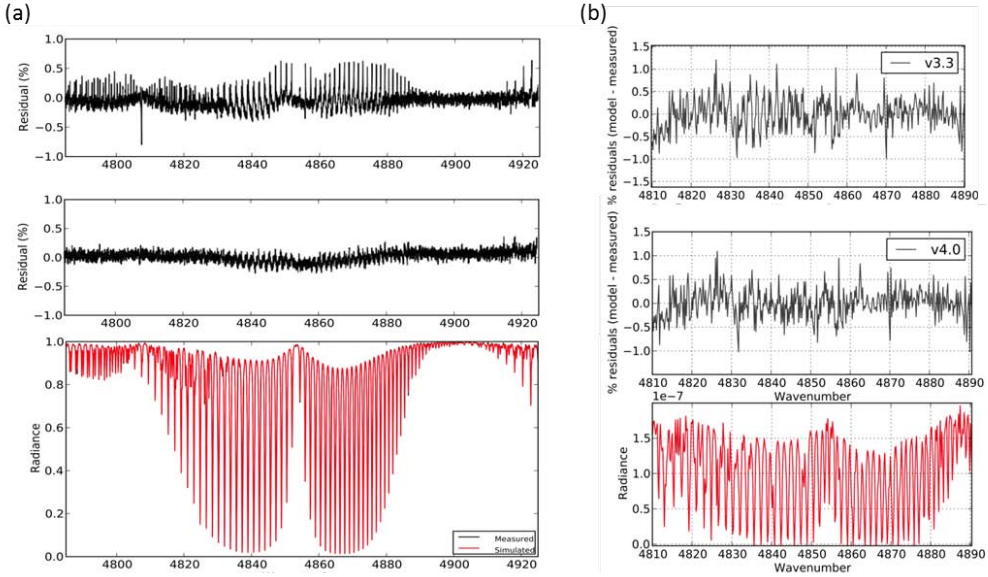

Fig. 5. **(a)** Spectral residuals in fits to laboratory spectra of the SCO2 band (bottom) for the absorption coefficients used here (top), and values from the more recently implemented multi-spectral fitting approach (center). **(b)** Same as **(a)** for TANSO-FTS spectra collected in the vicinity of the Lamont Oklahoma TCCON station.

AMTD
5, 1–60, 2012

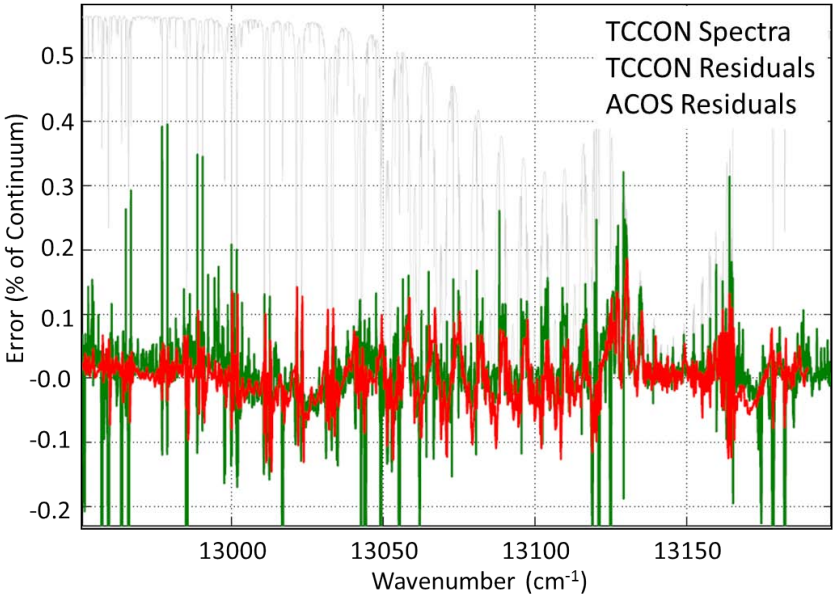

Fig. 6. Comparison of spectral residuals in the O_2 A-band from TCCON (green) and ACOS GOSAT (red) retrievals, along with a TCCON O_2 A-band spectrum (light grey).

AMTD
5, 1–60, 2012

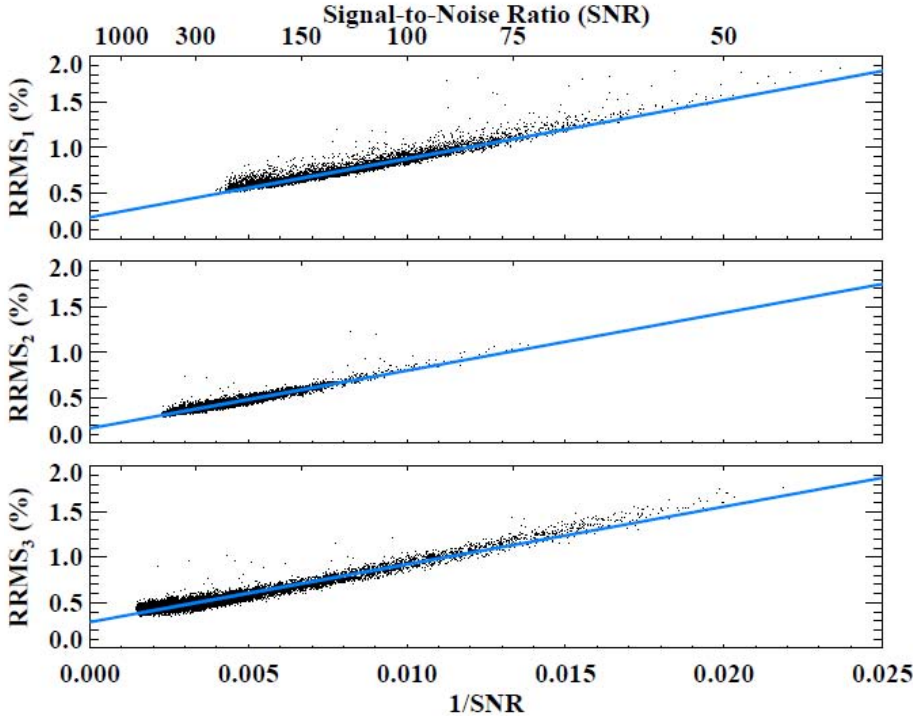

Fig. 7. Values of the relative root-mean-square (RRMS) of the residuals in the three TANSO-FTS SWIR bands are shown as a function of the inverse of the SNR for all GOSAT TANSO-FTS soundings collected over continents in July 2009 that converged, passed the cloud screen, and all other quality filters (black dots). A linear fit to each distribution of points is shown (blue line). If the RRMS were dominated by instrument noise or other random errors, the blue lines should go through the origin. The offset indicates the presence of systematic errors that do not decrease with increasing SNR. In B2.8, those errors are approximated as an "empirical noise."

AMTD
5, 1–60, 2012

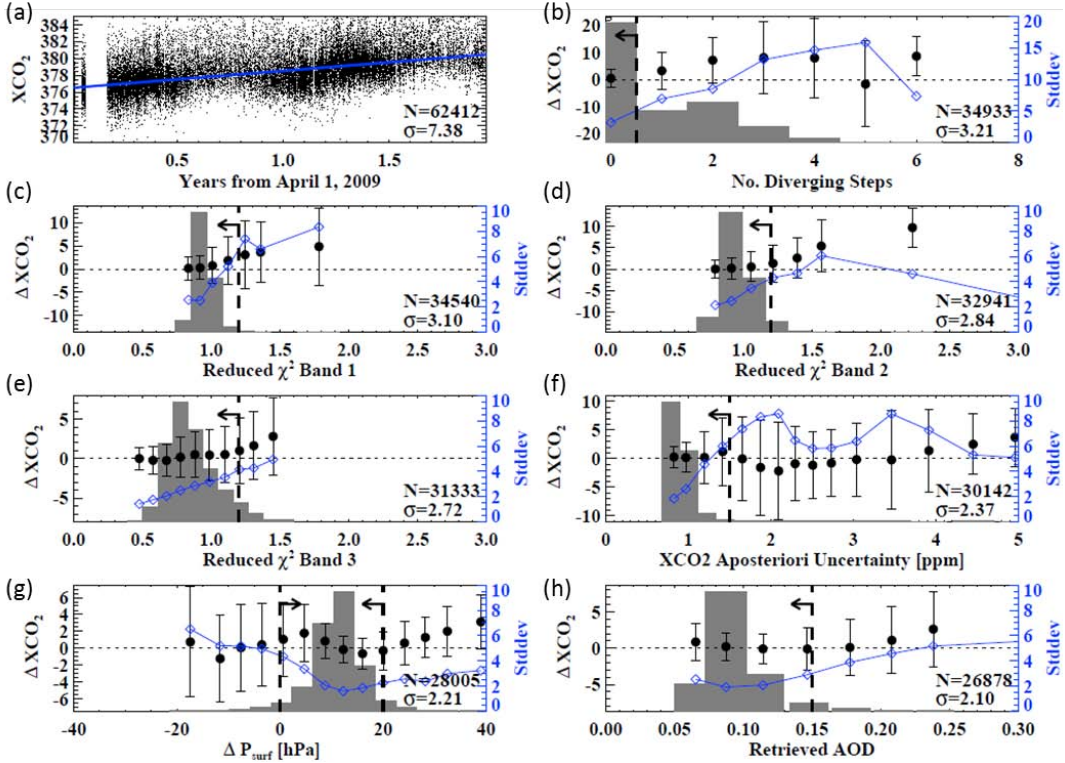

Fig. 8. Caption on next page.

AMTD
5, 1–60, 2012

Fig. 8. Derivation of the post-processing filters applied to ACOS B2.8 data products. **(a)** X_{CO_2} estimates from all cloud-free soundings collected over land at latitudes between 20° S and 70° S between 4 April 2009 and 19 April 2011. The blue line indicates the secular trend in X_{CO_2}. Other panels show a histogram of the distribution of soundings as a function of the filtering variable (grey boxes) as well as: (i) the difference between the ACOS GOSAT and mean TCCON X_{CO_2} estimates, ΔXCO_2, (black points with 1-σ error bars) for each bin in the histogram; (ii) the standard deviation in ΔXCO_2 for each bin in the histogram (blue diamonds and blue line, quantified as Stddev on the right-hand ordinate), and (iii) the range of values that pass the filter (dashed vertical lines with horizontal arrows). The number of points that passes the each filter, N, and the standard deviation in ΔXCO_2 for this ensemble,σ, are shown in the lower right of each panel. The filtering variables include the number of diverging steps in the retrieval **(b)**, the reduced χ^2 for the fit in the 3 SWIR bands **(c–e)**, the X_{CO_2} a posteriori uncertainty **(f)**, the difference between the retrieved and a priori (ECMWF) surface pressure, ΔP_{surf} **(g)**, and the total aerosol optical depth at 0.755 µm, AOD. The panels are shown with the cumulative effect of each previous filter applied, so that only soundings passing all previous filters are used in any given panel.

AMTD
5, 1–60, 2012

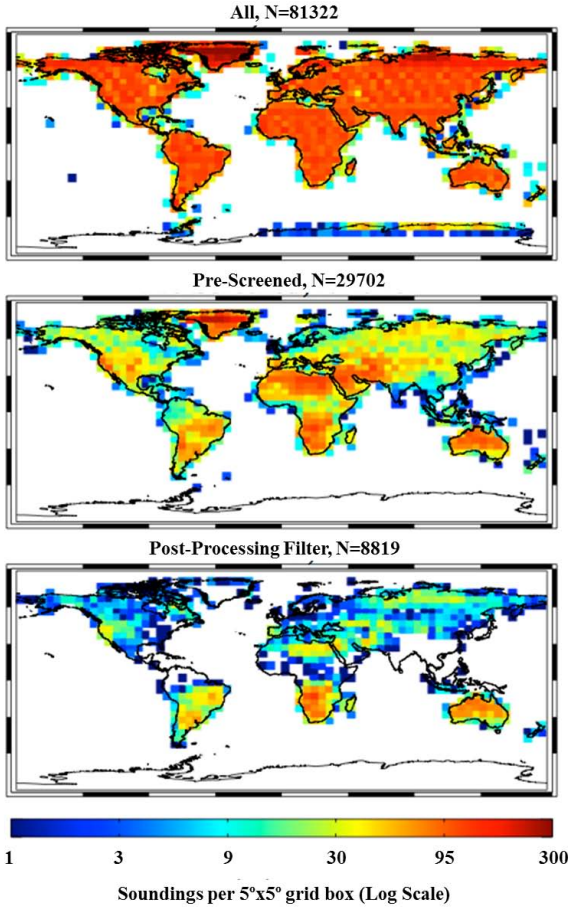

Fig. 9. The spatial coverage for all GOSAT TANSO-FTS soundings over land from July 2009 (top) is compared to that for soundings that pass the pre-screening (cloud and latitude) filters (middle) and all post-processing filters listed in Table 4 (bottom).

AMTD
5, 1–60, 2012

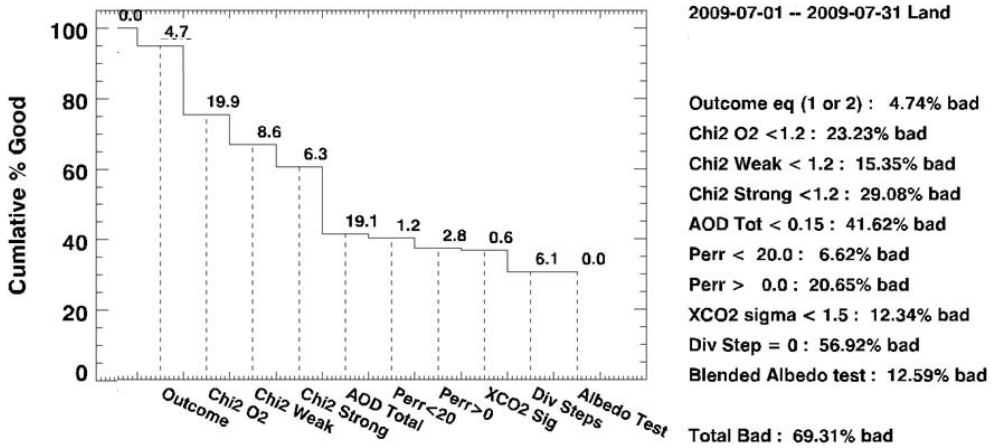

Fig. 10. Throughput of post-screening filters for July 2009. Histogram of reductions in the number of soundings by each step in the screening process (left) and the filter criterion and total fraction of the soundings that would be eliminated by each filter (right). The filters are applied from left to right, such that bad soundings are rejected by the first filter criterion that they fail.

AMTD
5, 1–60, 2012

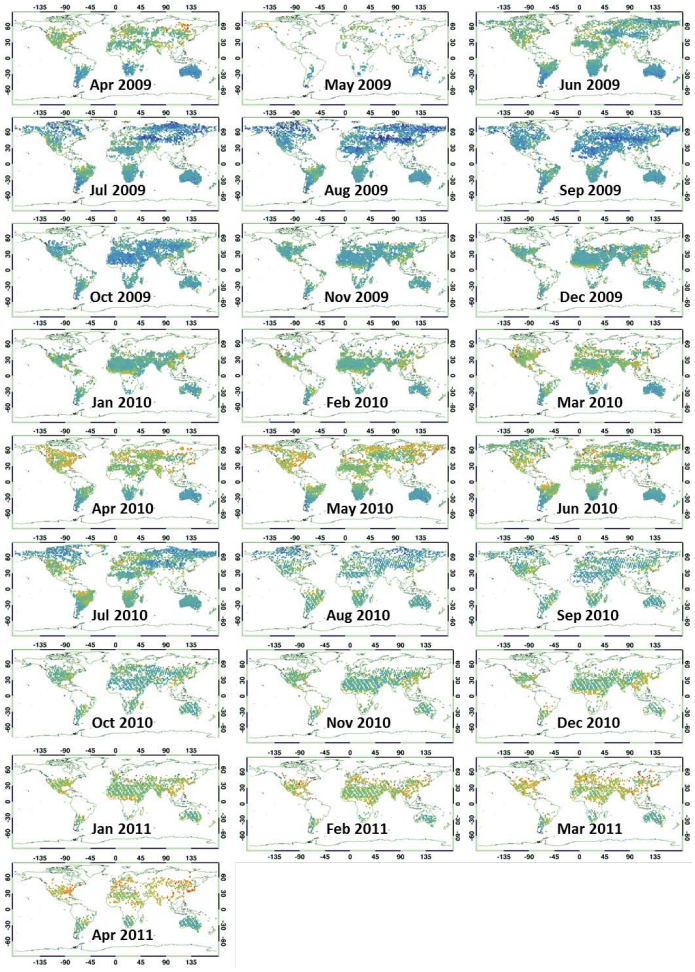

Fig. 11. Caption on next page.

AMTD
5, 1–60, 2012

Fig. 11. ACOS GOSAT B2.8 X_{CO_2} retrievals for April 2009–April 2011. Each map shows the X_{CO_2} values retrieved over a 1-month interval. Each symbol indicates the average of all X_{CO_2} estimates in a $2^{\circ} \times 2^{\circ}$ bin for that month that passed all pre- and post-screening filters. The coverage in May 2009 is limited because TANSO-FTS was still being commissioned and few soundings were collected. The data used to create the maps can be obtained from the NASA GES DISC.

AMTD
5, 1–60, 2012

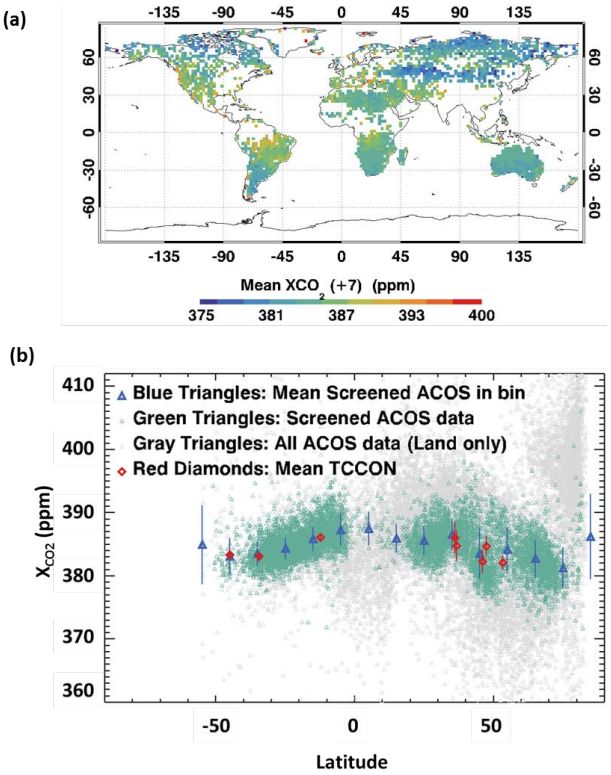

Fig. 12. **(a)** The ACOS GOSAT B2.8 X_{CO_2} estimates shown in Fig. 1 have been divided by 0.982 to remove the global component of the bias and improve their agreement with contemporaneous TCCON retrievals. **(b)** Map of all ACOS GOSAT B2.8 XCO2 soundings over land for July 2009 that passed all pre- and post-screening filters.

AMTD
5, 1–60, 2012

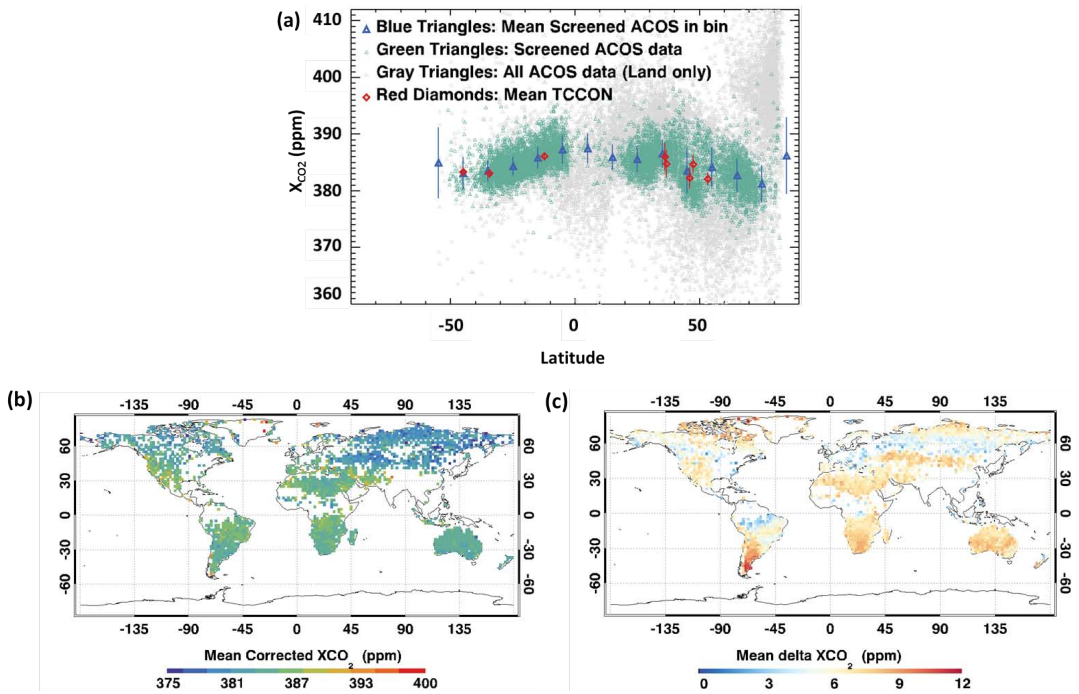

Fig. 13. ACOS GOSAT 2.8 retrievals from July 2009, corrected using the empirical regression formula developed by Wunch et al. (2011). **(a)** Corrected B2.8 soundings that pass the nominal B2.8 screens (green triangles) and their averages in 10° zonal bins (blue triangles) are compared to TCCON measurements (red diamonds). **(b)** Spatial map of corrected B2.8 soundings. **(c)** Differences between the X_{CO_2} retrievals shown in Fig. 13b and the raw B2.8 retrievals shown in Fig. 1. After removing a ~7 ppm global offset, the empirical correction yields reduced X_{CO_2} over the tropics and northern mid-latitudes and higher values elsewhere. The combination of relatively large solar zenith angles and the presence of snow and ice cover in Patagonia contribute to the large positive air mass and blended albedo corrections there.

AMTD
5, 1–60, 2012

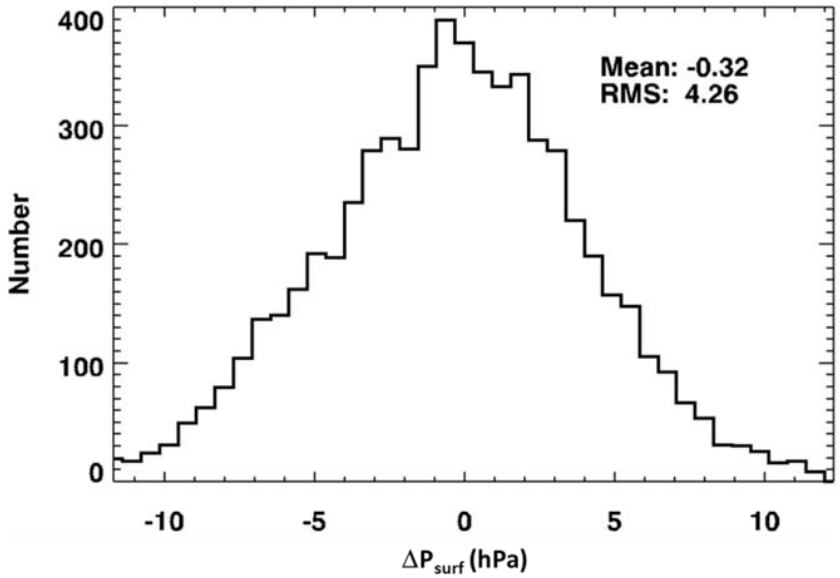

Fig. 14. Histogram of differences between the retrieved pressure and the ECMWF prior, ΔP_{surf} for sounding retrieved using scaled ABO2 absorption coefficients. The data set used here includes all soundings over land collected in 23–25 April 2009, 1–31 July 2009, 18–20 September, and 14–16 January 2010 that pass the 85° solar zenith angle and cloud screening tests. Rescaling the O_2 absorption coefficients largely eliminates the global bias and yields a standard deviation comparable to that assumed in the a priori covariance matrix (± 4 hPa).

AMTD
5, 1–60, 2012

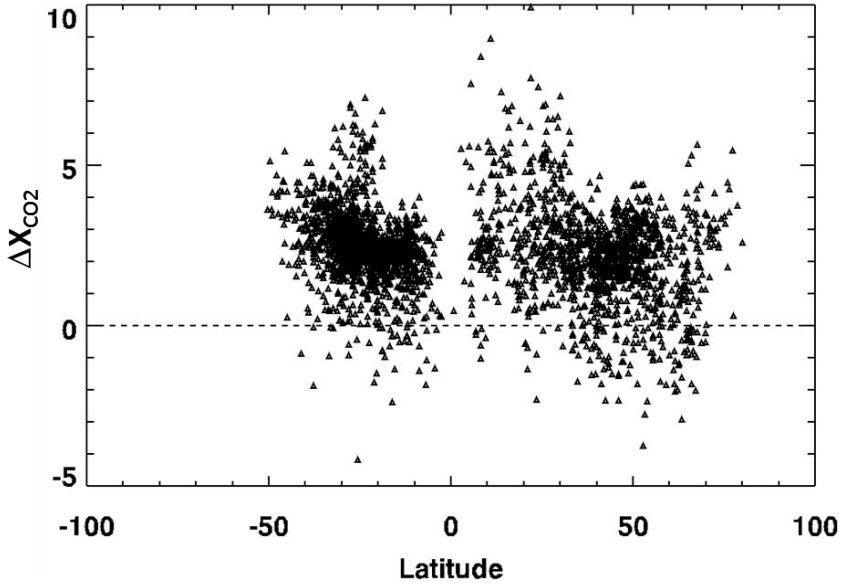

Fig. 15. Change in X_{CO_2} produced by correcting the ILS interpolation error recently identified in the B2.8.

AMTD
5, 1–60, 2012

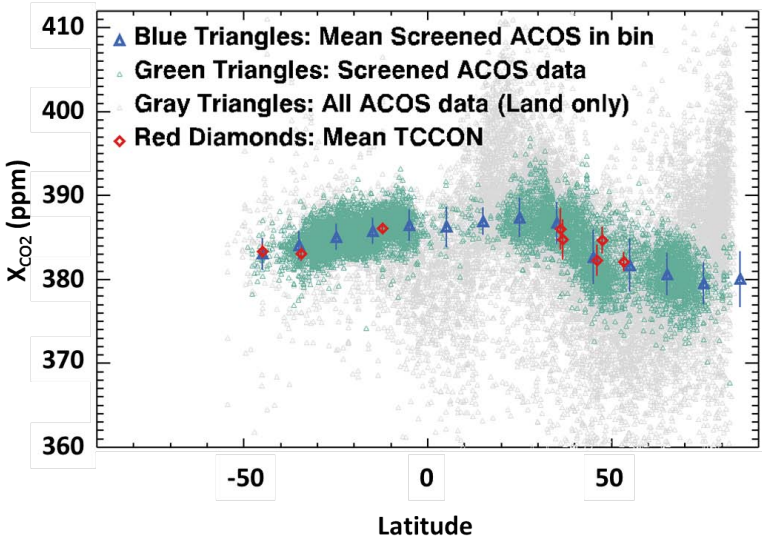

Fig. 16. Same as Fig. 1, but for ACOS GOSAT B2.9. This version of the algorithm incorporates scaled O_2 A-band absorption cross-sections, improved WCO2 cross-sections, corrected ILS interpolation, a zero-level-offset retrieval, and other improvements to yield a much better fit to the TCCON results at all latitudes.

AMTD
5, 1–60, 2012

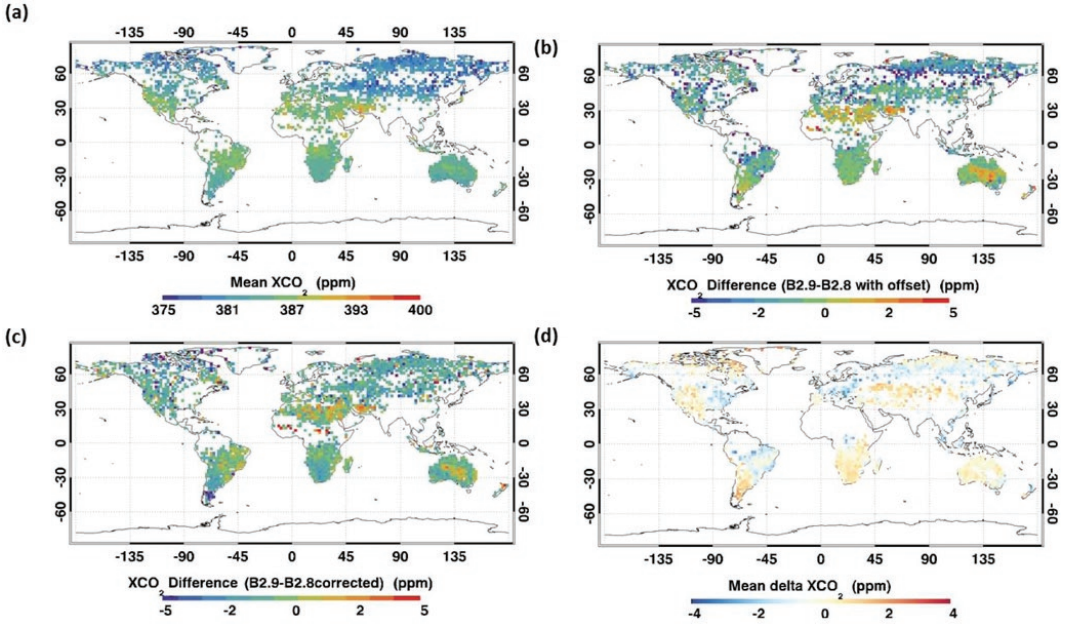

Fig. 17. Comparison of the preliminary B2.9 product with rescaled and corrected versions of the B2.8 product. **(a)** Map of the B2.9 product for July 2009, using the same post-processing filters used for the B2.8 results. **(b)** Difference between the B2.9 product and the B2.8 product, offset by ~7 ppm to remove the global X_{CO_2} bias. **(c)** Difference between the raw B2.9 product and the B2.8 results corrected for bias with the empirical approach developed by Wunch et al. (2011). **(d)** Differences between the the B2.9 results corrected for bias with the empirical approach developed by Wunch et al. (2011) and raw B2.9 product.

AMTD
5, 1–60, 2012